FABRICATION AND MECHANICAL PROPERTIES OF GRAPHITE FIBER REINFORCED ALUMINUM ALLOYS

by

KIYOYUKI ESASHI

B.E.(1967) and M.E.(1969), TOHOKU UNIVERSITY, JAPAN

A THESIS SUBMITTED IN PARTIAL FULFILMENT OF
THE REQUIREMENTS FOR THE DEGREE OF
MASTER OF APPLIED SCIENCE

in the Department
of
Metallurgy

We accept this thesis as conforming
to the required standard

THE UNIVERSITY OF BRITISH COLUMBIA

APRIL, 1976

In presenting this thesis in partial fulfilment of the requirements for an advanced degree at the University of British Columbia, I agree that the Library shall make it freely available for reference and study. I further agree that permission for extensive copying of this thesis for scholarly purposes may be granted by the Head of my Department or by his representatives. It is understood that copying or publication of this thesis for financial gain shall not be allowed without my written permission.

Department of Metallurgy

The University of British Columbia
2075 Wesbrook Place
Vancouver, Canada
V6T 1W5

Date Apr. 30 1976

ABSTRACT

A new method to fabricate continuous graphite fiber reinforced aluminum alloy composites has been developed and the tensile properties of the composites have been investigated. Composites with 601, 201 and 7178 alloy matrix containing up to 19 volume per cent of Thornel 50 graphite fiber were studied.

These composites showed lower tensile strength values than the expected values from the "rule of mixture". A theoretical model is discussed in order to understand the tensile properties of these composites. In this mechanism, graphite fibers are thought to be broken continuously one after another at maximum loading point of ultimate tensile strength during the tensile test.

A further attempt has been made to improve the tensile strength of these composites, based on the above theoretical work.

TABLE OF CONTENTS

Page

LIST OF FIGURES

LIST OF TABLES

ACKNOWLEDGEMENTS

The author gratefully acknowledges the helpful discussions with his research director, Professor E. Teghtsoonian, and with Dr. J.S. Nadeau.

He wishes to thank the members of the faculty and fellow graduate students of the Department of Metallurgy for their continued support and interest in this work.

Financial assistance was received in the form of an assistantship under National Research Council of Canada grant number A-2452, and is gratefully acknowledged.

I INTRODUCTION

I-1. General Background

Over the past 15 years, much research has been carried out in attempts to realize in practice the greater potential of high performance fiber reinforced composites. The fiber reinforcement has been considered for the strengthening of weak plastic materials, such as resin and some metals. The incorporation of strong fibers into ductile metal matrices has been shown to bring remarkable increases in the strengths of these metals by some theoretical and experimental work of the early period in the metal matrix composite history.

An important simple expression for the composite tensile strength and tensile modulus, so called "rule of mixture", was derived in such work (1) and it has been quite often used to discuss the tensile properties of various kinds of fiber composites. In this "rule of mixture", the tensile strength and tensile modulus of a composite are expressed as the combination or summation of contributed amounts from fibers and the matrix, to these properties. These contributions from each component are taken to be proportional to their volume fraction in the composite. This rule was derived assuming the overall fracture of fibers at the same time. The detail of this expression is discussed in a later section, IV-1.

Metal matrix composites are distinguished from the extensively developed resin matrix composites by virtue of their metallic properties. The main advantages of metal matrix as compared with resin matrix are summarized as follows:

a) The strength of metals is greater than resins

b) Metals have higher tensile modulus than resins

c) Metals possess electrical conductivity and the thermal conductivity of metals is higher than resins

d) Metals possess greater high temperature strength.

Commonly used resins possess tensile strength values of $7-15 \times 10^3$ p.s.i. and tensile modulus of $0.4 - 0.7 \times 10^6$ p.s.i. The density of resin (1.25 gr/cc) is very low compared with metals, so that points a) and b) are not definite advantages of metals when the composites are used for weight critical applications. Resin matrix composites are available only for room temperature use. Therefore, a definite advantage of metal matrix composites for structural material is their high temperature capacity.

I-2. Previous Work on Fabrication Techniques

Various kinds of fiber composite fabrication techniques have been developed so far. These fabrication methods can be classified as shown in Table 1. Most of these methods, except the unidirectional solidification method of eutectic alloys, are thought to be combinations of two processes, the fiber alignment process and the consolidation process. In the consolidation process of these fabrication methods, hot pressing (H.P.) and liquid phase hot pressing (L.P.H.P.) techniques are commonly adopted in order to prevent fiber damage. Most of these methods are not used for commercial composite production because of the cost or because of certain problems in each method as mentioned in the following pages; however, they are applied to fabricate composite specimens shown as examples in this table, successfully only for experimental purposes. The application of the plasma spraying method for SiC coated boron filament aluminum matrix composites is a representative example of commercial

Table 1. Fabrication Techniques of Metal Composites

Method of Fiber Alignment	Applied Examples: Matrix	Applied Examples: Fiber	Method of Consolidation	Reference
Deposition				
Chemical Vapor Deposition	Al	Graphite Fib.	H.P., L.P.H.P.	2
	Ni,NiCr	Al_2O_3SiC Whisk.	H.P.	3,4
Electro Co-Deposition	Ni	Al_2O_3SiC Whisk.	C.P., H.P., L.P.H.P.	3,5
Electroplating	Al	Graphite Fib.	H.P.	6
	Al	Boron Fil.	H.P.	7
	Ni	Al_2O_3SiC Whisk.	H.P.	3,7,8
Electroless Plating	Ni	Graphite Fib.	H.P.	9,10
	Co	Graphite Fib.	H.P.	10
Plasma Spraying	Al(Alloy)	Boron Fil.(SiC Coated)	H.P.	11,5
	Ti	Boron Fil.	H.P.	5
Metal Matrix				
Unidirectional Solidification of Eutectic Alloy	Al	Al_3Ni	Solidification	12,13,14
	Cb	Cb_2C		15,16
	Zn	$Zn_{15}Ti$		17,18
	Ni	W		19,16
	Co-Cr	$(Cr,Co)_7C_3$		20,16
	Ni_3Al	Ni_3Ta		21,16
	Ni	NbC		22,16
Infiltration	Al(Alloy)	Graphite Fib.	Solidification of Matrix	23,24,25
	Ag	Al_2O_3 Whisk.		26,1,3
	Al(Alloy)	Al_2O_3 Whisk.		27,3
	Ni(Alloy)	Al_2O_3 Whisk.		7,3
	Cu	W Wire		28,1
	Al	Boron Fil.		31

Method of Fiber Alignment	Applied Examples: Matrix	Fiber	Method of Consolidation	Reference
Solid State Matrix				
Extrusion of Powder Matrix	Al	Short Graphite Fib.	Diffusion Bonding	29
	Al	Si_3N_4 Whisk.		3
	Hastelloy	W Wire		7
Alternate Pile up of Metal Foil & Fibers	Al	Graphite Fib.	L.P.H.P.	30
	Al	Boron Fib.	H.P.	7,32
	Ti-6Al-4V	Boron Fil.	H.P.	7
Clad Wire (matrix block with holes for wires)	Ti-6Al-4V	Be wire	Mechanical Deformation and Diffusion Bonding	33
Slurry or Slip of Powder Matrix				
Spinning, Extrusion	Ag,Fe,Ni	Si_3N_4 Whisk.	Burn Off Organic Component and H.P. or L.P.H.P.	34,3
Drawing of Mixture of Metal Powder, Whisker and Carrier Solution	Al Alloy	Sic whisk.		35,3
	Cu,Mg	Sic whisk.		36,3
Filtering Slurry and Settling out of Ni-coated Whiskers and Matrix Powder in Magnetic Field	Ni,Cr	SiC Whisk.	L.P.H.P.	38,3
	Al Alloy	Al_2O_3 Whisk.		37,3

productions (11).

The chemical vapor deposition method seems to be the most expensive process among other methods in this table. This process usually involves the use of halide gas of the matrix metal, so that there is a limitation on the variety of applicable matrix metal for this process. The number of fibers in a bundle which is produced in this process is also limited. In order to obtain a uniform coating film on fiber surfaces, good penetration of the gas into the bundles is necessary.

The electro co-deposition, electro plating and electroless plating methods often form small pores in the metal matrix when rather fine fibers like whiskers of graphite fibers are used. Solution is often trapped in these pores, so that it is rather difficult to eliminate these pores by the subsequent consolidation process.

The plasma spraying method can be adopted only for large diameter continuous fibers like boron fibers (11). Melted metal powder is sprayed continuously on the fibers aligned on a thin tape of the same metal.

The unidirectional solidification method of eutectic alloys has been extensively studied because of the high potential to produce high temperature resistance metals for gas turbines etc. (39). Not only the fibrous eutectics, such as $(Cr,Co)_7C_3$ reinforced (Co, Cr) eutectic alloy, Ni_3Ta reinforced Ni_3Al alloy and NbC reinforced Ni alloy, but also the lamellar eutectics, such as $Ni_3Al(\gamma')$-$Ni_3Nb(\delta)$ eutectic alloy were reported to possess higher strength and more creep resistance than the so-called "super alloys" (16). These types of composites have been expected to be suitable for high temperature applications because of the thermodynamic stability in the eutectic systems and the small effect of grain boundaries due to their large columnar structures. This process has advantages of easy fabrication; however, the alloys are limited to

the eutectic alloys which can form suitable second phase and the volume fraction of reinforcements is limited consequently. The infiltration method is used for composites using small diameter fibers. The matrix metal must have good wetting property with the fiber in this method. In order to prevent the degradation of fibers by chemical attack, the proper control of infiltration condition is necessary. Graphite fiber aluminum alloy composites were successfully fabricated by this method (23)(24)(25).

The powder matrix extrusion process tends to damage fibers. The matrix foil process is suitable for rather large diameter fibers which can be easily handled and aligned. It seems to be difficult to increase the fiber volume fraction of composites and control the fiber spacing uniformly by this method, especially in the case of fine fibers like graphite fibers. Clad wire process can be used only for ordinary metal wire of high ductility.

Finally, two methods based on metal powders in an organic solution were developed to align fine whiskers in a matrix with little damage to them. In the first method, the green composites are fabricated into a strand shape by some mechanical deformation, such as extrusion. The organic components of the slurry are burned off prior to hot pressing.

In the second method, green composites are fabricated into the shape of a mat by settling out and filtering the slurry. Prior to the settling process, whiskers are coated with magnetic metal in order to permit high alignment of these whiskers by magnetic force during the process. This process seems to have some difficulties to obtain uniform distribution of fibers through the total thickness of the mat because of a large difference in the settling speed of these two materials.

Boron fibers have already been successfully incorporated into metals such

as aluminum, magnesium and titanium. The applications of these composites are limited to special fields because of their high cost. The main potential advantage for graphite fiber composites is the much lower fiber cost. As a matter of fact, large amounts of graphite fibers have been used in resin matrix composites, such as golf club shafts and turbine blades which must have high stiffness (Young's modulus) - weight ratio. The future progress of graphite fiber metal matrix composites greatly depends on the development of reliable and low cost fabrication techniques.

It is very difficult to fabricate metal matrix composites with graphite fibers because of the small fiber diameter (6-9μ) compared with boron fibers (100-125μ). The alignment and consolidation processes for such fine fiber composites have to be carefully designed in order to prevent any mechanical fiber damage. The chemical attack at the fiber-matrix interface may also give severe damage to the fine fibers, if the fabrication process involves high temperature operations. As a matter of fact, nickel, cobalt and steel dissolve graphite at high temperature and degrade the fibers. Copper is expected to be a good matrix because of the low carbon solubility; however, not many studies have been done with copper due to its high density relative to aluminum, and its limited range of high temperature use comapred with nickel and cobalt.

In recent years, aluminum or aluminum alloys have been thought to be the most promising matrix for graphite fibers because of the high strength and stiffness to density ratio. Aluminum is one of the carbide forming elements; however, the graphite fiber aluminum composites are expected to be used safely at the practical long time service temperature which is much lower than the carbide formation temperature (>500^{o}C).

Aluminum carbide formation on the surface of PAN Type II* fibers in pure aluminum composites produced by powder metallurgical process was first observed and measured by G. Blankenburgs (29), using a quantitative X-ray technique. Fig. 1 and 2 show the carbide formation of various temperatures and various times.

P.W Jackson (40) also studied PAN Type I*fibers coated with aluminum by chemical vapour deposition. Tests on specimens held at 500^{o}C for one day exhibited no noticeable loss in room temperature strength of the coated fibers. On the other hand, the apparent degradation of the coated fibers at higher temperature than this was recognized as shown in Fig. 3. It was concluded that the fiber degradation was caused by the chemcial attack of the fiber surface by aluminum at such high temperature.

Such chemical reaction suggests good wetting between these materials. The infiltration process was finally applied to Thornel 50 graphite fiber 13% silicon aluminum alloy composites successfully by R. Pepper, J. Upp, R. Rossi, and E. Kendall (23) (25). This process has been expected to be a practical fabrication process because specimens fabricated by this process exhibit much higher values than any other fabrication process and sometimes even higher values than the values according to the "rule of mixture". The real reason for this remarkable strength increase is still unknown.

Although many kinds of high modulus graphite fibers are being produced by manufacturers, only a few have been used for metal matrix composites. They can be classified into some categories, of which properties are shown together with other reinforcing materials in Table 2.

---

*(Type II: High strength type; Type I: High modulus type).

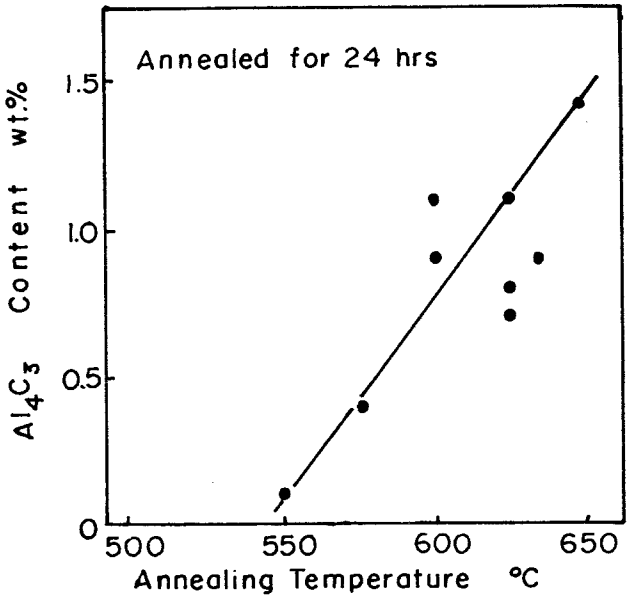

Fig.1. The Variation of Al_4C_3 in 5 wt% Graphite Fiber - Aluminum Composite after Annealing for 24 hr at Various Temperatures (Determined by Quantitative x-ray Diffraction) (29).

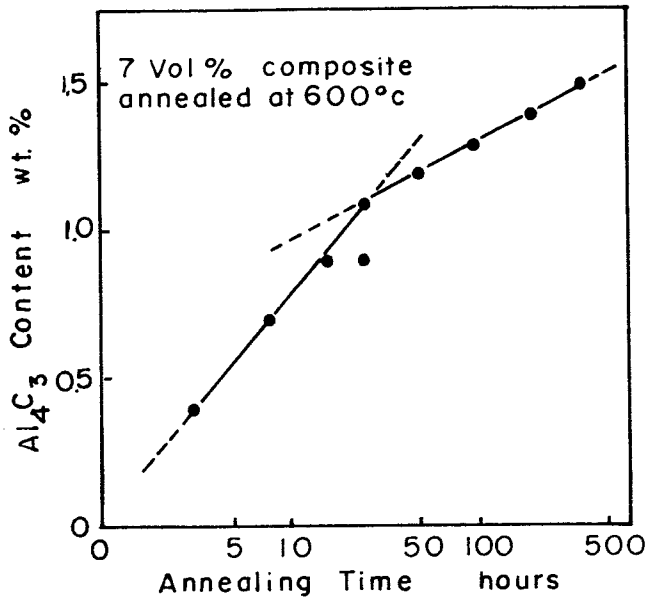

Fig.2. The Variation of Al_4C_3 in 5 wt% Graphite Fiber - Aluminum Composite after Annealing for Various Times at 600°C (29).

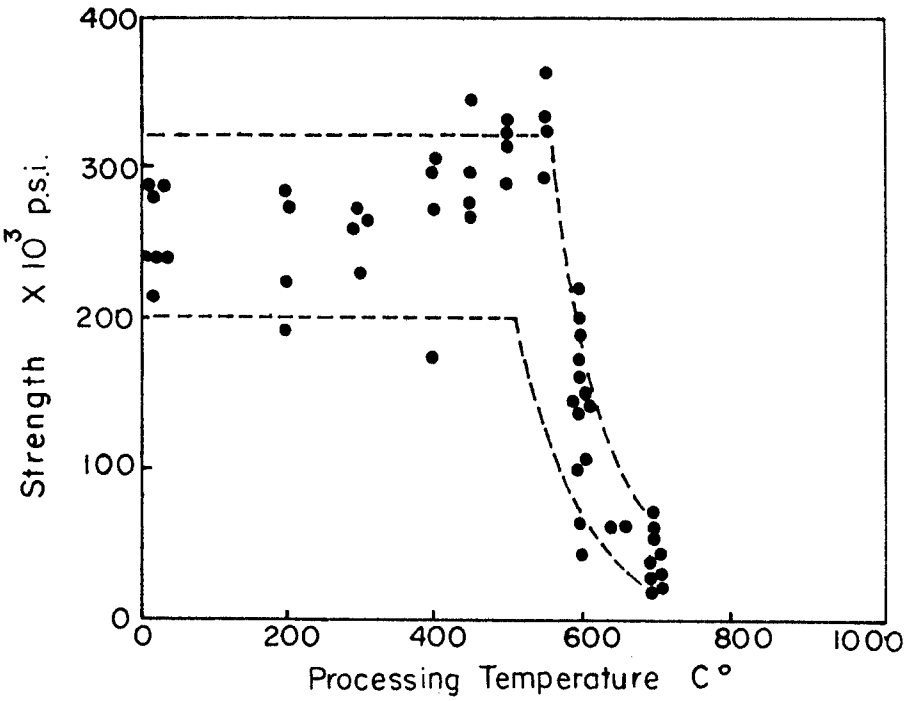

Fig.3. Strength of Al Coated Graphite Fibers after Heat Treatment for 1 Day at Various Temperatures (40).

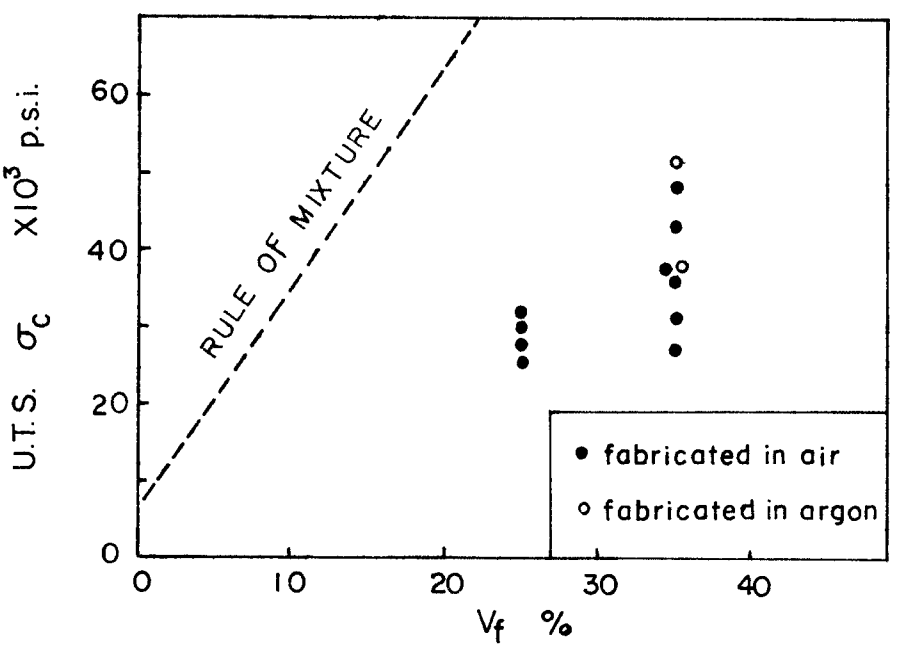

Fig.4. Tensile Strength of the Al-Graphite Fiber Composites Fabricated by the Matrix Foil Method. (Plotted from numerical data in Ref.30).

Table 2. Typical Properties of High Modulus Graphite Fibers Compared with Other Reinforcing Materials.

Reinforcement	Ultimate Tensile* Strength x 10^3 p.s.i.	Tensile* modulus x 10^6 p.s.i.	Density lb/in.^{3}	Diameter μ
Graphite Fibers				
Rayon-base				
Thornel 50	275 — 320	44 — 55	0.06	6.6
Thornel 75	350 — 385	70 — 80	0.065	6.0
PAN-base				
Type I (High modulus type)	225 — 275	55 — 60	0.072	7–9.7
Type II (High strength type)	325 — 375	32 — 38	0.063	7.6–8.6
Other Reinforcements				
Boron filament	400 — 500	55 — 60	0.092	100-150
Beryllium wire	150 — 200	35 — 40	0.066	100-250
Tungsten wire	550 — 600	48 — 52	0.7	50-100
Aluminum whisker	4000	62	0.14	1–10
Silicon carbide whisker	3000	70	0.12	1–10

(* Measured on single fibers).

I-3. Previous Work on Strength of Graphite Fiber Aluminum and Alloy Composites

A study on graphite fiber aluminum composites was reported by A. Morris (30). Specimens were fabricated from PAN Type II fibers and aluminum foils, using a liquid phase hot pressing technique. The ultimate tensile strength values, σ_c, as a function of fiber volume fractions of these composites are plotted in Fig. 4. The values are highly scattered and considerably lower than the expected values from the "rule of mixture".

P. Jackson et al. (2) fabricated PAN Type II fiber aluminum composite specimens by the chemical vapour deposition process, using Tri-isobutyl aluminum. The tensile strengths of these composites are shown in Fig. 5, for various fabrication conditions, as a function of the fiber volume fraction. In spite of considerable effort to satisfy the requirements of low porosity, minimum chemical attack, minimum fiber breakage and uniform fiber distribution, the tensile strengths of these composites were well below "rule of mixture" levels. On the other hand, the tensile modulus of these composites were generally close to the expected values. It was suggested that a further mechanism was operating in keeping strength levels down.

Pepper et al. (23) (25) fabricated samples by the infiltration technique as mentioned earlier. After multiple chemical washing, Thornel 50 graphite fiber bundles were infiltrated in a batch process with 13% silicon aluminum alloy. The mean tensile strength value of 106 x 10^3 p.s.i. was obtained with 28% fiber volume fraction and this value was unaffected by 20 thermal cycles between -193^{o}C and 500^{o}C. As mentioned earlier, this value compares favourably with that expected from a "rule of mixture" calculation.

In their following studies, pure Al, Al-7Mg, Al-7Zn and Al-13Si alloys were used to fabricate composites with Thornel 75 graphite fibers. The results

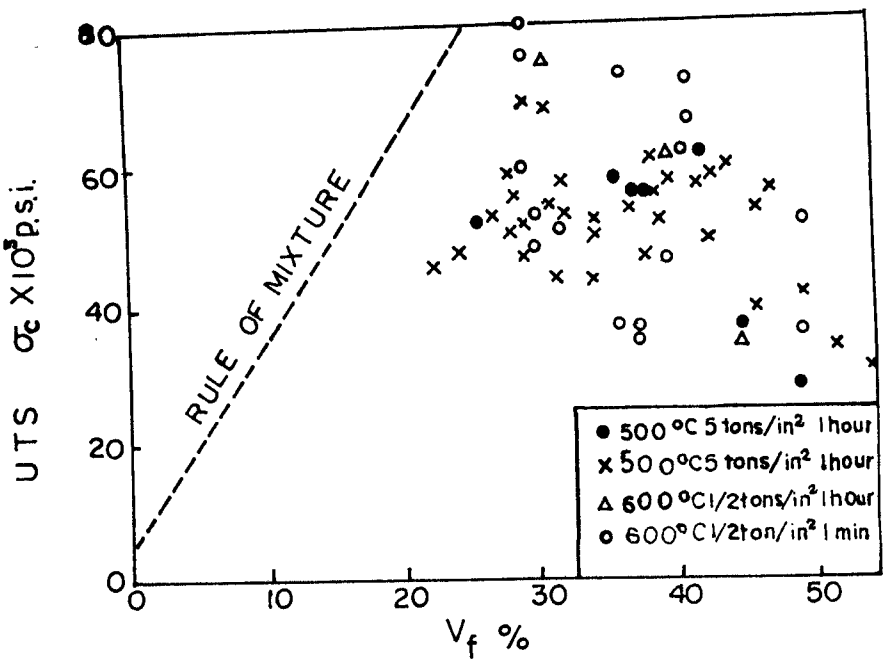

Fig.5. Tensile Strength of Graphite Fiber Aluminum Composites Fabricated by the Chemical Vapour Deposition Method (2).

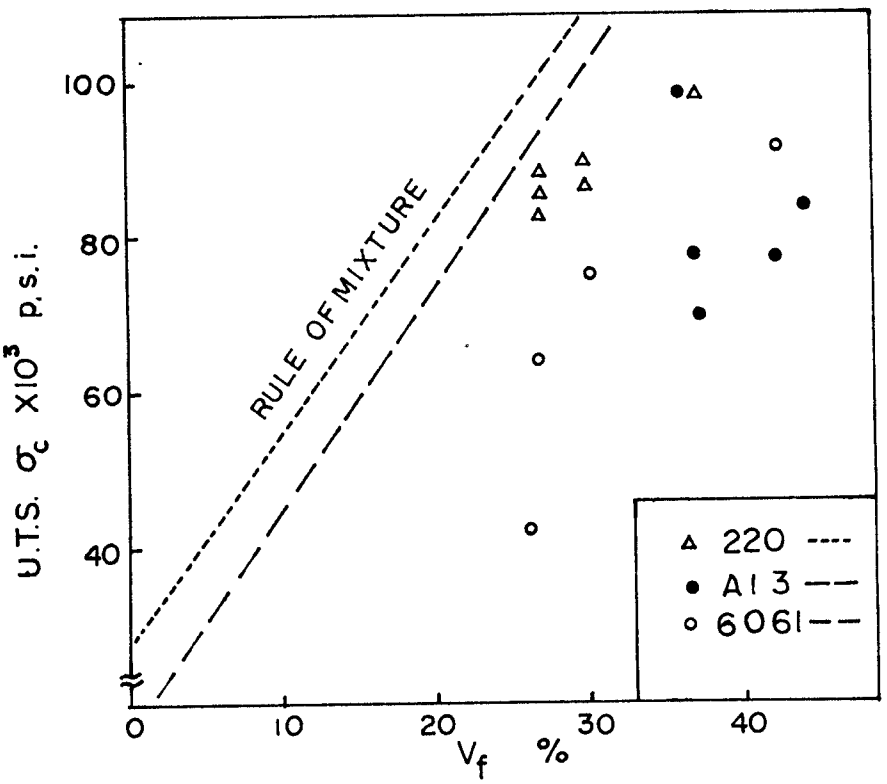

Fig.6. Tensile Strength of Graphite Fiber Aluminum Alloy Composites Fabricated by the Infiltration Method. (Plotted from numerical data in Ref.24).

of this work are shown in Table 3. The tensile strength values are again lower than "rule of mixture" values and scattered very much.

Further work on the composites of continuously produced infiltration composite strand was done by R. Pepper and R. Penty (24), using Al-13Si (A13), Al-10Mg (220), and Al-1Mg-0.6Si (6061) alloys with Thornel 50 graphite fibers. The tensile strength values are again lower than the "rule of mixture" values and still scattered in very wide region as shown in Fig. 6.

These composites fabricated by infiltration process usually possess higher ultimate tensile strength than the composites by other processes; however, the distribution of the fibers in the matrix of the infiltrated composites is not uniform. This non-uniformity seems to originate in the hot pressing die configuration which involves the use of filler metal foils among composite wires as shown in Fig. 7 (25).

The fiber distribution of these composites must be seen as a bundle structure.

I-4. Purpose of Present Work

The infiltration technique of aluminum alloys developed by R.T. Pepper et al. led to remarkable progress in the fabrication of graphite fiber aluminum composites.

The major advantage of this process includes low fabrication costs, minimum fiber damage, and potentially high strength. The achievement of uniform fiber distribution is difficult, making theoretical modeling awkward.

The strength values actually achieved are scattered in a very wide range and much lower than the theoretical values calculated according to the "rule of mixture".

Table 3. Tensile Properties of Various Aluminum-Alloy-Thornel 75 Composites (25)

Matrix Composition	Specimen Condition	Volume Percent Fiber	Strength		Number of Samples	Low Value (psi)	High Value (psi)	Average Modulus	
			Average						
			MN/m^2	p.s.i.				(GN/m^2)	(psi)
Commercially-pure aluminum	As-infiltrated	32	68	99,000	8	65,000	116,000	178	25.7
	Pressed	35	65	95,000	7	85,000	104,000	147	21.3
Aluminum-7 w/o zinc	As-infiltrated	32	71	103,000	7	59,000	132,000	166	24.1
	Pressed	38	87	126,000	10	102,000	155,000	190	27.5
Aluminum-7 w/o magnesium	As-infiltrated	31	68	98,000	4	87,000	124,000	195	28.1
Aluminum-13 w/o silicon	As-infiltrated	22	55	80,000	7	73,000	88,000	165	23.8

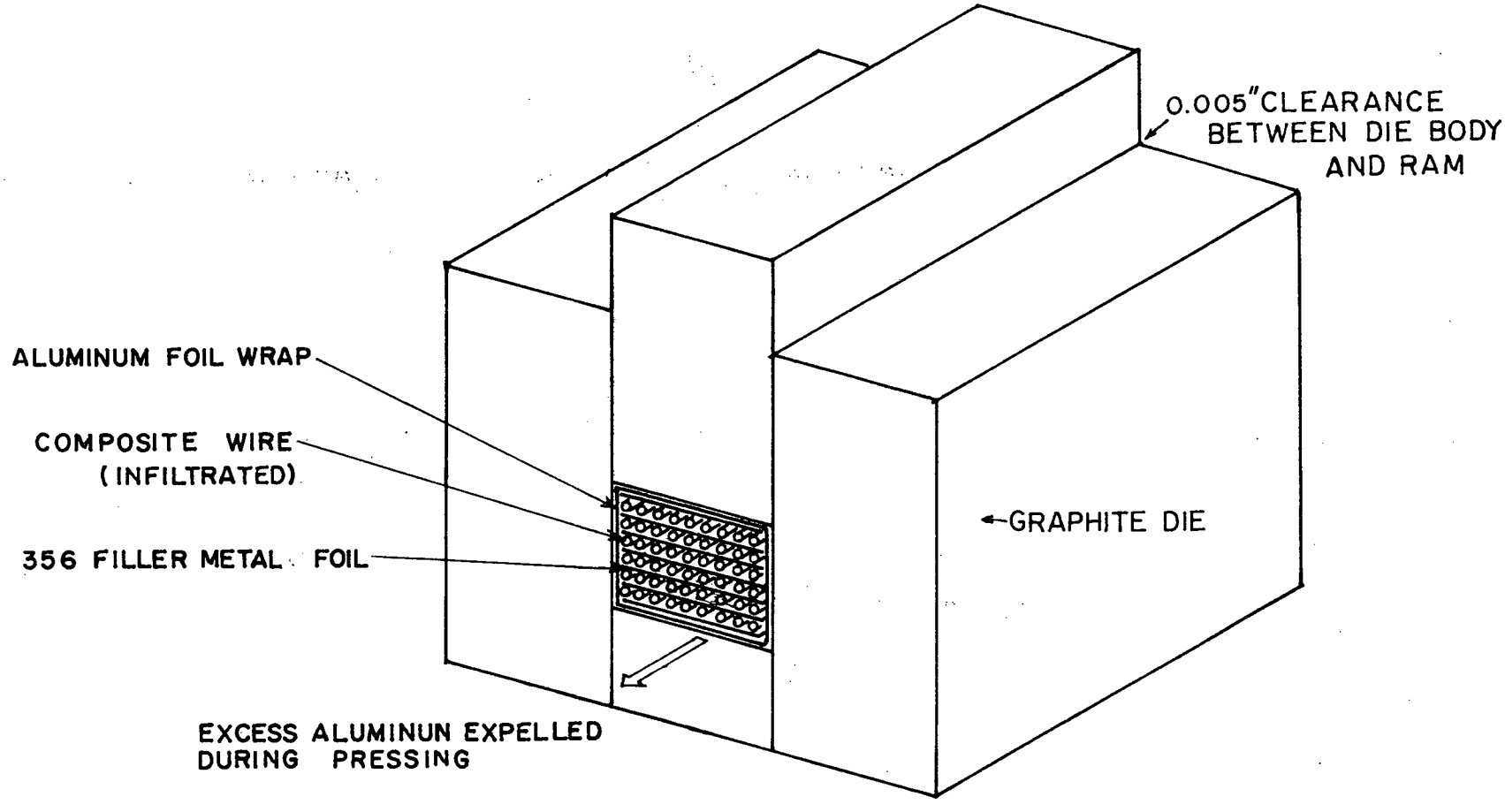

Fig.7. Liquid Phase Hot Pressing Die Configuration to Fabricate Specimens from the Al Infiltrated Graphite Fiber Composite Wire (25).

The reason for the difference between experimental results and theoretical values has not yet been fully understood. A different mechanism from the "rule of mixture" might be operating on the tensile fracture of these graphite fiber aluminum composites. The purpose of the present work is to investigate the mechanical behaviour of the composites and to make a theoretical model which can correlate with this behaviour.

II EXPERIMENTAL PROCEDURE

II-1. Preparation of Composite Specimens

Three kinds of aluminum alloys were chosen as matrices of the composite. Their nominal compositions are tabulated in Table 4.

The composites were fabricated by a unique method which was designed to obtain statistically or macroscopically homogeneous fiber distribution in the matrix. The statistical homogeneity of fiber distribution is necessary for the present work on fiber strengthening mechanism. The overall fabrication process in this method is outlined in Fig. 8.

Blended powders of each alloy composition were prepared from under 500 mesh powders of aluminum, silicon, magnesium,and copper shown in Fig. 9. These blended powders were mixed well together with denatured alcohol to make a powder suspended thin slip.

Thornel 50 graphite yarns were washed in boiling distilled water for about two hours to dissolve the P.V.A. coating film applied by the manufacturer in order to reinforce the yarns and avoid their degradation during handling. After the fibers were dried and untwisted, they were bundled and the top of the bundles were glued with epoxy resin. The number of fibers in each bundle was varied from 76,000 to 228,000 depending on the fiber volume fractions which were desired in the final product. The number of fibers in one bundle is limited by geometrical factors related to the diameter of the outer glass tube. Too many fibers prevent their free movement and adequate separation during the subsequent powder penetration. On the other hand, some bundles were prepared from original twisted yarns without untwisting them in order to obtain bundle structure fiber distributions in the matrices.

Table 4. The Nominal Composition of Matrix Alloys

Alloy	Heat Treatment	Mg %	Si %	Cu %	Zn %	Al %
601	T4 (Solution Treatment)	at. 1.11 wt. 1.00	at. 0.58 wt. 0.60	at. 0.11 wt. 0.25	-	at. 98.20 wt. 98.15
201	T6 (Age Hardened)	at. 0.46 wt. 0.40	at. 0.79 wt. 0.80	at. 1.92 wt. 4.40	-	at. 96.84 wt. 94.40
7178	T6 (Age Hardened)	at. 3.15 wt. 2.70	-	at. 0.80 wt. 2.00	at. 2.95 wt. 6.80	at. 93.00 wt. 88.50
Density of Each Element, $^{g}/_{cc}$		1.74	2.32	8.96	7.14	2.70

Table 5. Properties of Thornel 50 Graphite Fiber

Tensile Strength* p.s.i.	$275 - 320 \times 10^3$
Tensile Modulus* p.s.i.	$44 - 55 \times 10^6$
Density $^{g}/_{cc}$	1.66
Elongation at Break %	0.6
Equivalent Diameter μ	6.6
No. of Fibers/ply	720
Plies/Yarn	2

(* Measured on Single Fibers)

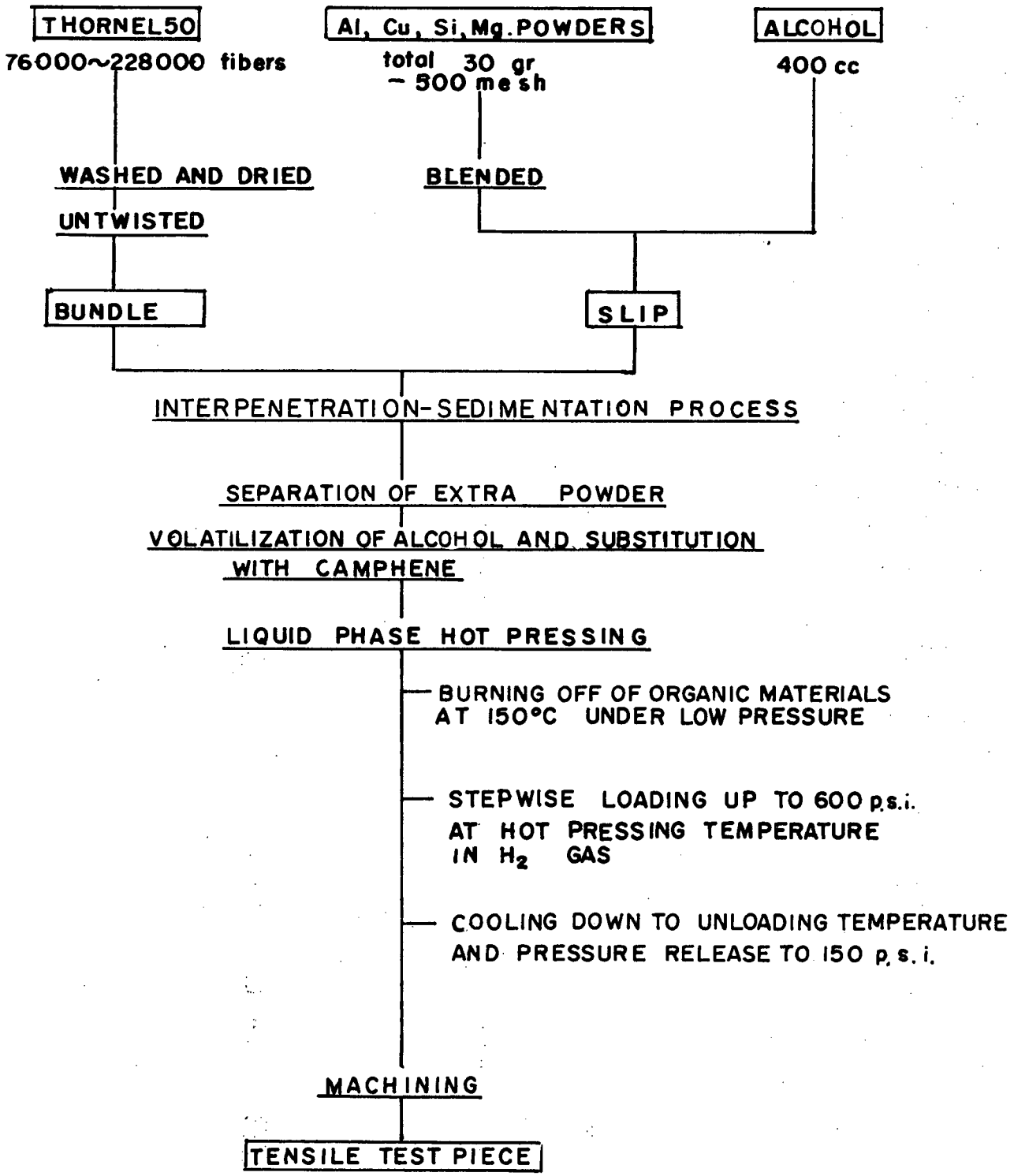

Fig.8. Flow Sheet of the Specimen Fabrication Process

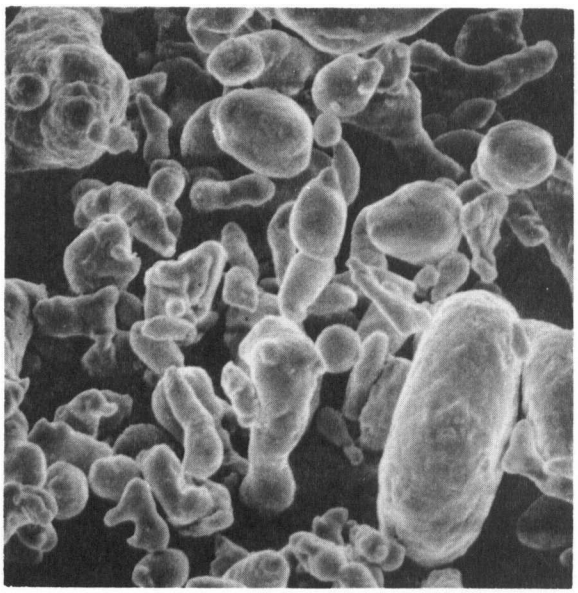

(a) Aluminum

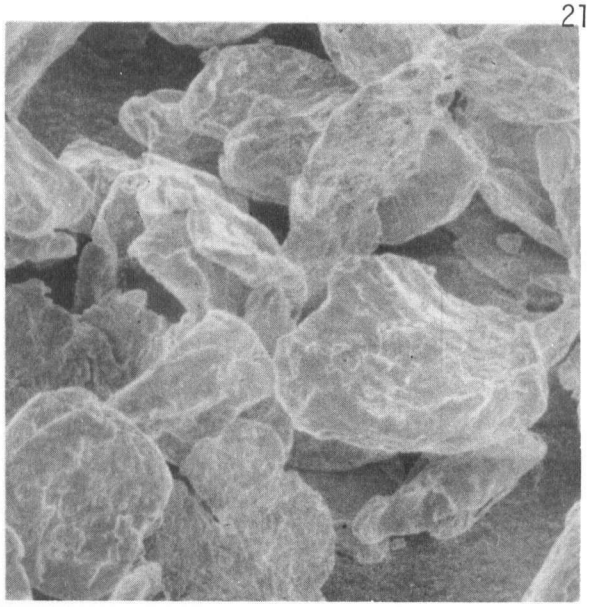

(b) Magnesium

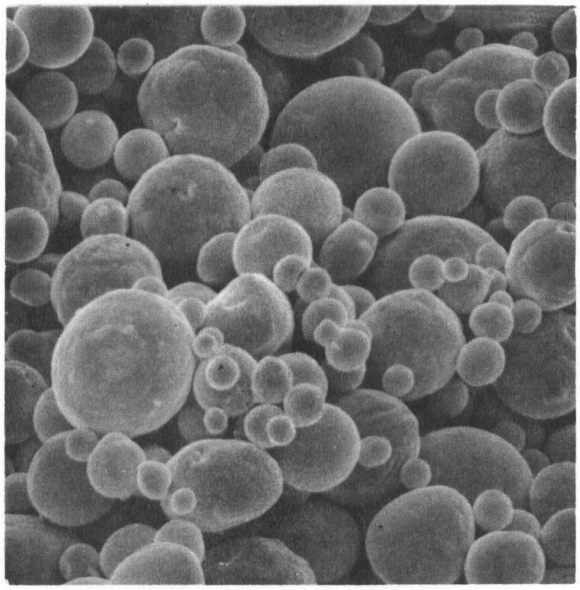

(c) Copper

Fig.9. Scanning Electron Micrographs of the Powders Used, x 1000

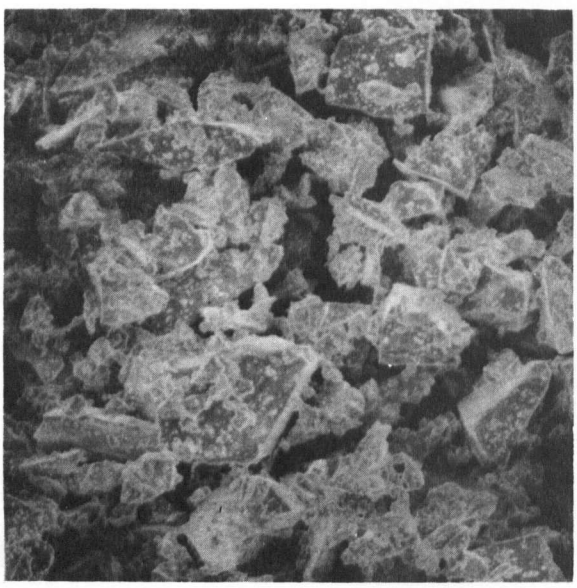

(d) Silicon

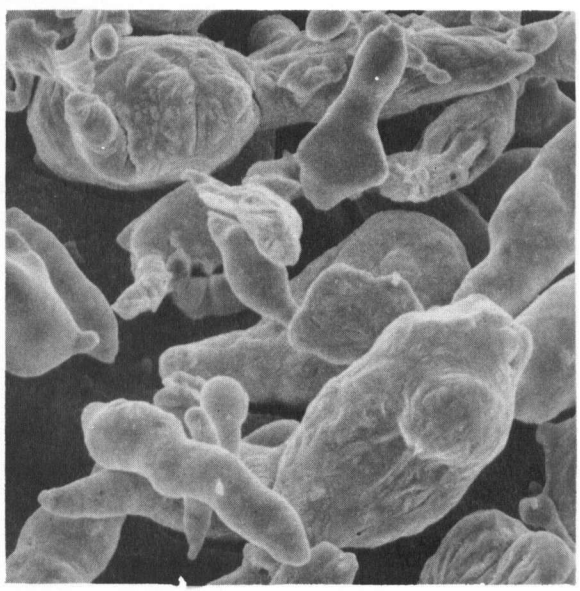

(e) Zinc

The fiber bundles were interpenetrated with the blended powder slips using a device designed specially for this purpose. This device is schematically shown in Fig. 10. The outer glass tube (A) is filled with the slip after a fiber bundle (B) is connected to a rod (C) with a spring (D) and inserted into a glass sheath (E) which moves up gradually from the bottom of the bundle to the top with vertical vibration during the operation. A drive and vibrator assembly at the top of the unit causes vertical vibration of both the connecting rod and the glass sheath.

The powder starts to interpenetrate into the bundle and settle among the fibers opened by these vibrational movements of the rod and the sheath tube. The slow upward movement of the sheath tube makes more complete interpenetration of the powder particles among the fibers possible. After sedimentation of the powder particles proceeds, additional charge of slip is poured into the glass tube three or four times.

Green composites which were produced by this operation are pushed out from the outer glass tube. These green composites contain more powder at the boundary of the original plies than at the inside, because, even if the plies are untwisted, they still have a tendency to twist back and keep the original twisted form slightly. To remove the extra powder particles from these areas, the green composites are transferred to a vibrating boat containing a small amount of alcohol (see Fig. 11). The distribution of fibers among the powders becomes more uniform by this separation treatment. This process is repeated a few times, turning the specimens upside down until the amount of flowed out powder becomes very little.

The green composites are then transferred on to a flat plate to be pressed into a rectangular section. Alcohol was half evaporated and Camphene was infiltrated into the green at around $50^{o}C$ in order to reinforce the green com-

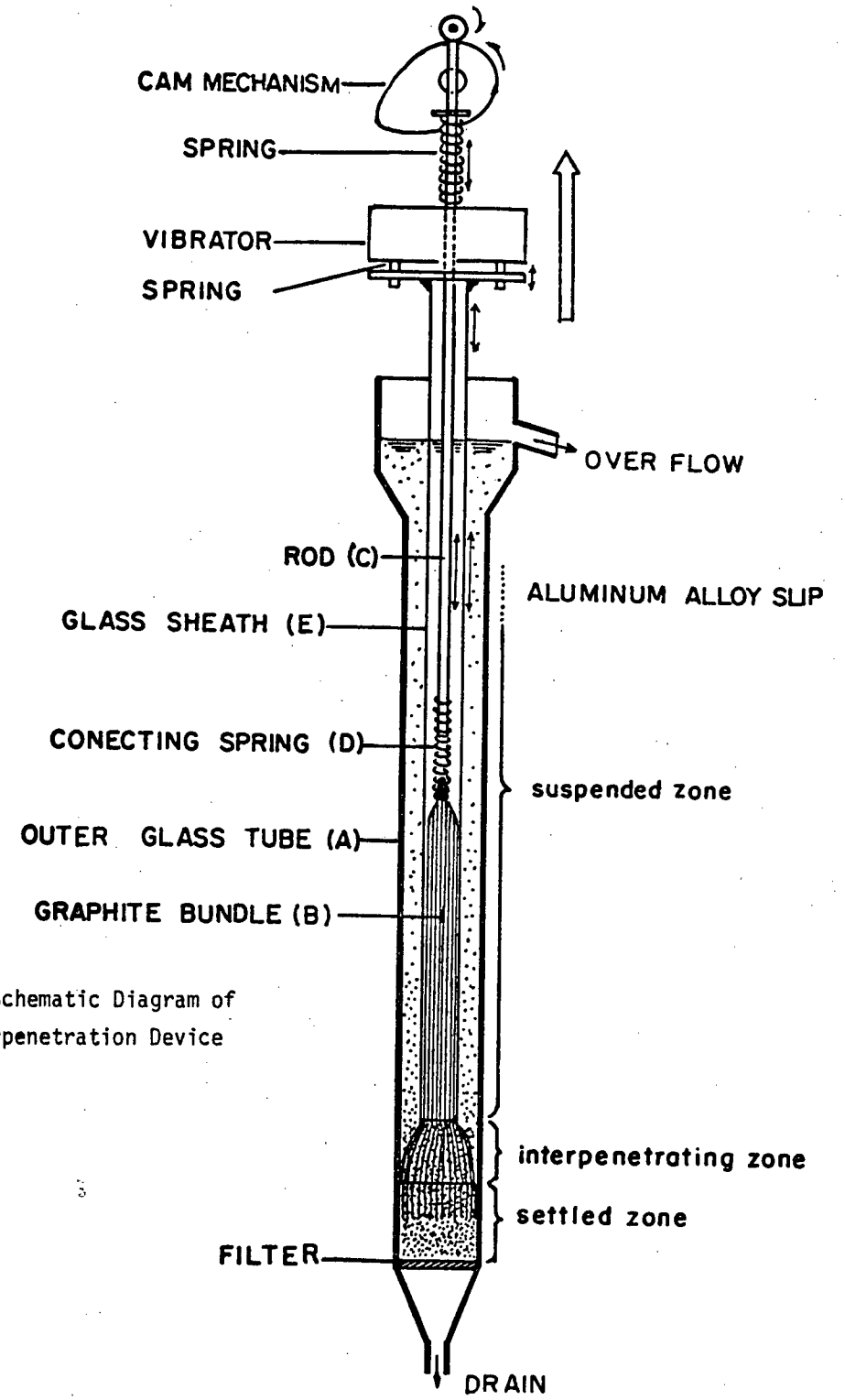

Fig.10. Schematic Diagram of the Interpenetration Device

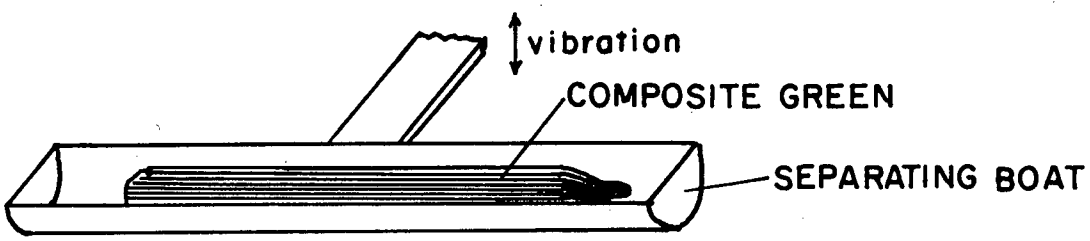

Fig.11. Separating Boat

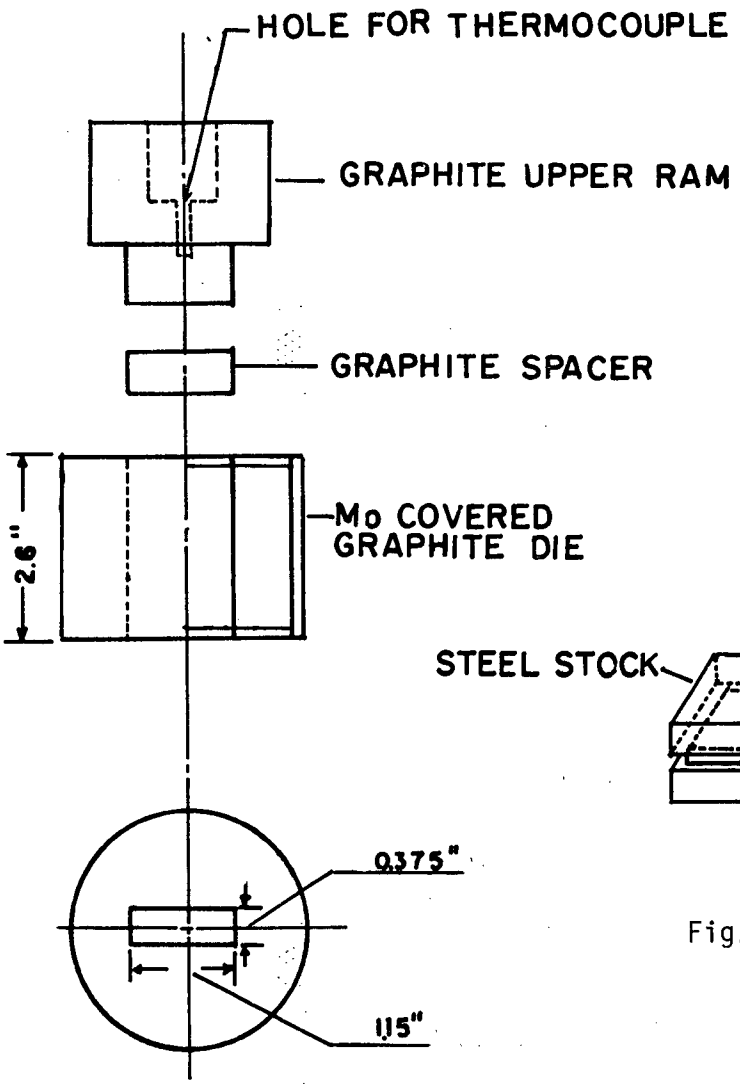

Fig.12. Hot Pressing Die Set

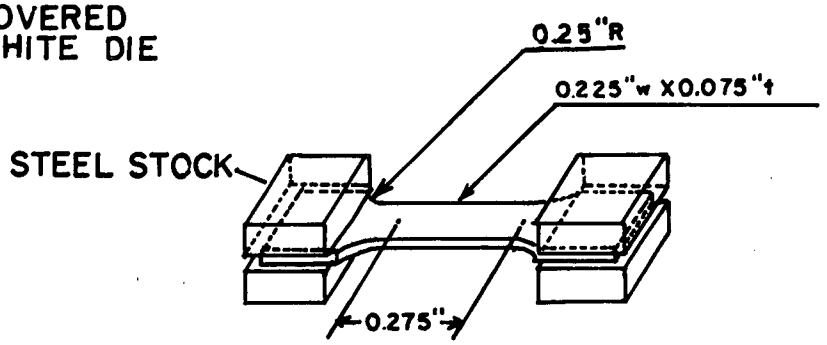

Fig.13. Tensile Specimen Geometries

posite; (however, this process is not necessary if half dried green composites are handled very carefully in the following processes because such composites have enough strength for handling as long as they are wet). The composites were cut into short lengths to fit the hot pressing die shown in Fig. 12, and pieces which contained defects were abandoned. All of the numerical values of factors in this fabricating process are tabulated in Table 6.

These pieces of green composites were then hot pressed in following process. The organic constituent was gradually evaporated under low pressure at around 150^{o}C in the die which was set in a hot pressing chamber. The degree of degassing was checked by a thermal gauge. After this degassing treatment, pressure was applied stepwise at the rate of 25 psi/min. at the temperatures shown in Table 7, in hydrogen gas atmosphere until the maximum pressure 600 psi was obtained. The contents of the die were kept at these temperatures under the pressure of 600 psi for one hour. During this period, partial melting of the powder occurs forming a liquid phase which easily infiltrates among fibers. Unreinforced alloy blanks were also fabricated in this hot pressing process from blended powders. These blank specimens were used to obtain a basis for fiber strengthening effect.

These hot pressed composite or blank specimens were then machined to the shape of tensile test specimens and heat treated to acquire different mechanical properties. The temperature and time for each alloy are also tabulated in Table 7. Steel stocks were attached to these heat treated specimens with Eastman Kodak 910 in order to protect the specimens from the grips of the tensile test machine, as shown in Fig. 13.

Table 6. Numerical Values of Controlling Factors in Interpenetration Process

Weight of Blended Powders in Slip for one charge	30 gr
Volume of Alcohol in Slip for one charge	400 cc
Number of Plies in a Bundle	100 — 300
Moving Speed of Sheath	About 6 inch/hr
Frequency and Amplitude of Bundles Vertical Vibration	60 c/s. 0.2 inch
Frequency and Amplitude of Sheath	60 c/s. 0.05 inch
Diameter of Sheath	9mm x 7 mm
Diameter of Outside Glass Tube	14mm x 12 mm

Table 7. Hot Press and Heat Treatment

	601T4	201T6	7178T6
Hot Pressing Temperature and Time	600°C, 1 hr	550°C, 1 hr	550°C, 1 hr
Pressure Releasing Temperature	500°C	450°C	450°C
Solution Treatment Temperature and Time	520°C,30 min	505°C,30 min	470°C,15 min
Ageing Temperature and Time		160°C, 18 hr	125°C, 28 hr

II-2. Tensile Testing

Tensile tests at room temperature were carried out with an Instron testing machine at the cross head speed of 0.02 inch/min, using self tightening grips. The tensile strength was determined for these specimens. Due to the very small elongation of the composite specimens (under 1%), it proved to be very difficult to establish the elongation at failure.

More accurate stress strain curves and longitudinal elastic modulus of several typical specimens were obtained using strain gauge on specimen surfaces.

II-3. Microscopic Observations

After the fracture surfaces were ground and polished, photographs were taken at a magnification of 114 times. The area covered by these pictures is around 1/7 of the original area on the specimen. The volume fraction of fibers in each composite was calculated using the numbers of the fibers counted in these pictures and a nominal value for fiber diameter (6.6μ).

Fracture surfaces and polished longitudinal sections were observed with a scanning electron microscope.

The surface of a 201-T6 composite specimen was polished prior to tensile testing and the deformation mode just before failure was observed by optical microscopy.

II-4. Micro Probe Analysis

The matrix composition of all specimens was analysed by means of micro probe analysis. Two counts at each of four points were carried out in the sections previously used to count the number of fibers. Regions of the matrix which had been liquid during the hot pressing were avoided in order to obtain representative values.

The tensile test data from specimens which showed too much deviation of composition from average values were excluded in order to improve the reliability of the data.

The big scatter of composition among specimens is due to the large density difference of each of the elements. This was expected since blended powders were used in the interpenetration process instead of alloy powders. The densities of these elements are tabulated in Table 4.

III EXPERIMENTAL RESULTS

III-1. Fiber Volume Fraction

The volume fraction of graphite fibers in each specimen was calculated using pictures as shown in Fig. 14. Fig. 15 shows the bundle structure of the 7178 T6 alloy composite which was prepared from original twisted yarns (1.5 turns/inch).

The fiber volume fraction of each specimen is tabulated together with the number of plies which were used to prepare each specimen in Table 8. The average fiber volume fraction is shown plotted against the number of plies per bundle in Fig. 16.

III-2. Micro Probe Analysis of the Specimens

The matrix chemical composition of each specimen was analysed by micro probe measurement and calculated using the "Magic" program. Wide scattering of analysed composition was found as anticipated earlier.

In order to avoid uncertainties arising from variations of matrix composition, limits were established (see Table 9) for allowable compositions. All specimens listed in Table 8 lie within these established limits.

III-3. Tensile Stress Strain Curves

Most of the stress strain curves were obtained directly from the Instron recorder. A limited number of stress strain curves was obtained by measuring the strain with strain gauges attached to the specimen surfaces.

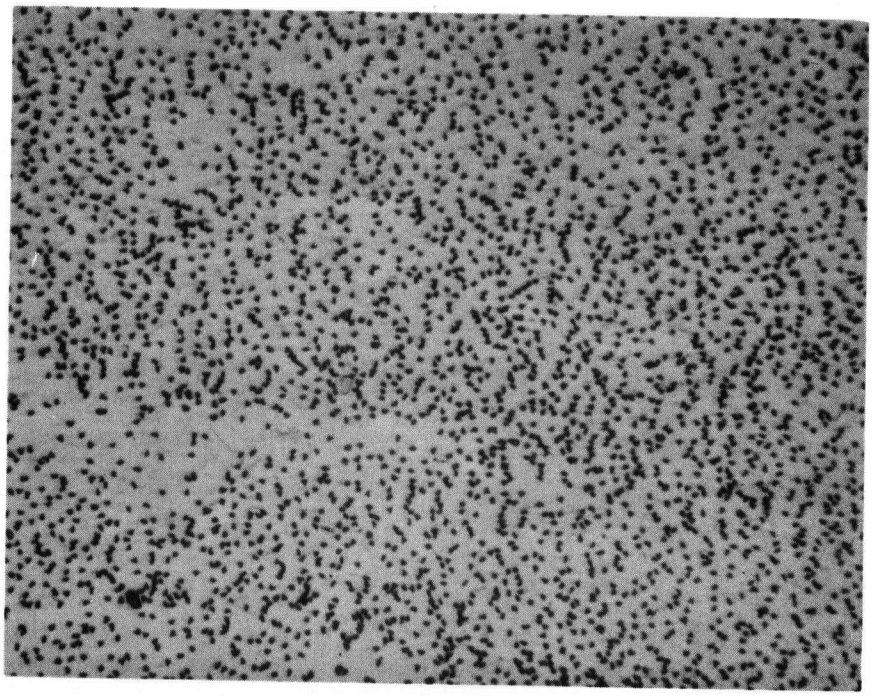

Fig.14. Cross Section of a Uniform Composite, 201T6, #29, 12.1% V_f, x 114.

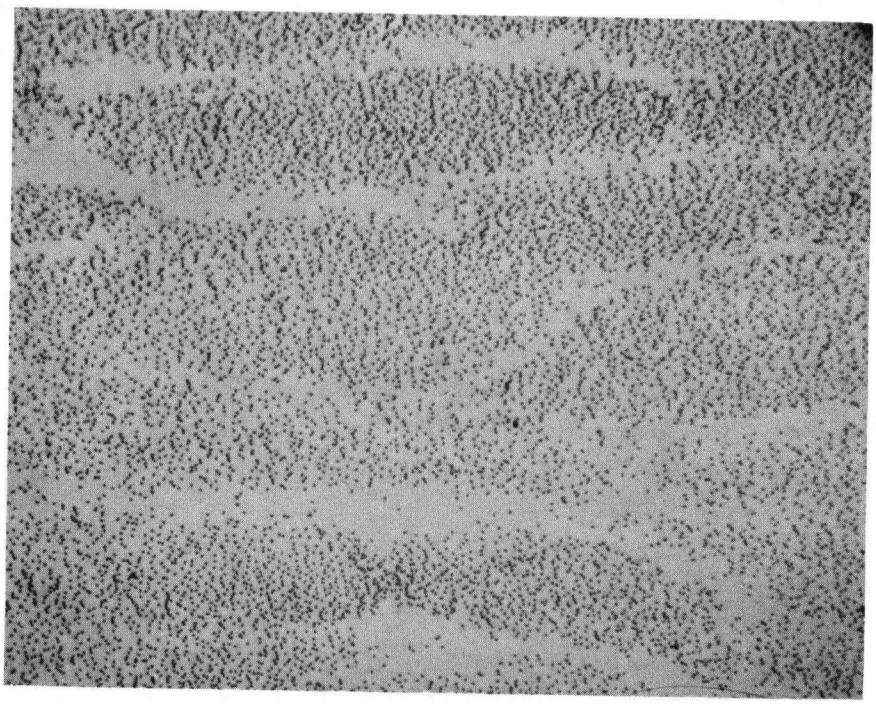

Fig.15. Cross Section of a Bundle Structure Composite, 7178 T6, #39, 10.0% $\bar{V}_f$, x 62.

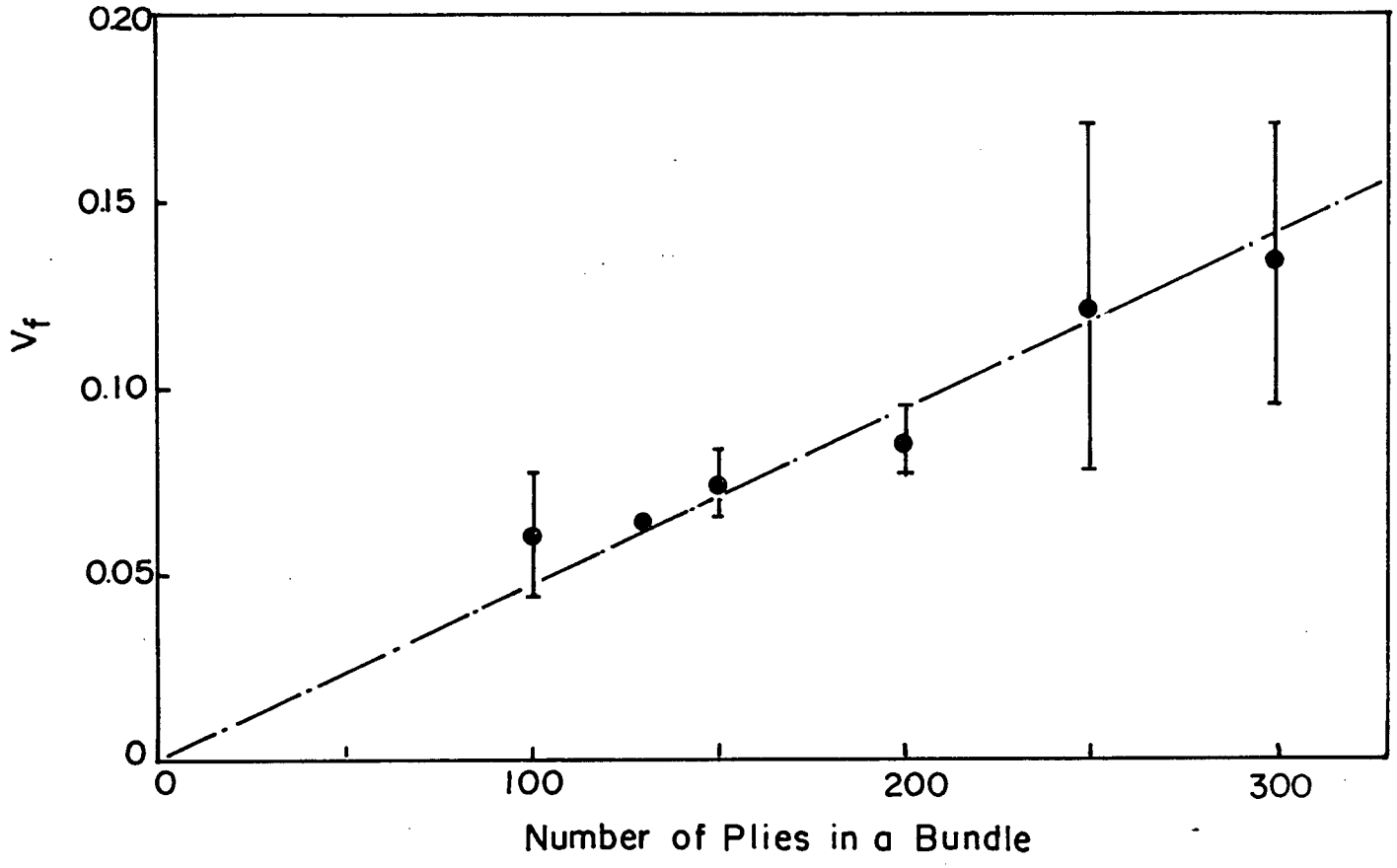

Fig.16. Relation between the Number of Plies for the Interpenetration Process and the Fiber Volume Fraction in Composites. The dot-dash-line shows the ideal correlation.

Table 8. Tensile Test Data of Specimens

Specimen No.	Alloy	Number of Plies	Fibre Volume Fraction, V_f	Composition, atomic% Mg%	Si%	Cu%	Zn%	Ultimate Tensile Strength $\sigma_c \times 10^3$ p.s.i.	Strain Gauge Measurement $\epsilon_{fail}, \sigma_\epsilon, E_c$
1	601T4	0	0	0.9	0.59	0.07		33.8	
2	601T4	0	0	1.04	0.50	0.09		29.9	
3	601T4	0	0	0.78	0.49	0.06		32.1	
4	601T4	0	0	0.87	0.51	0.10		32.8	$\sigma_{0.6}=18\times10^3$psi
5	601T4	100	4.3	0.89	0.58	0.09		29.0	
6	601T4	100	7.8	0.65	0.47	0.09		33.3	
7	601T4	150	6.5	1.00	0.47	0.12		31.4	
8	601T4	150	6.7	0.82	0.61	0.11		31.6	
9	601T4	200	8.5	0.94	0.58	0.10		33.6	
10	601T4	200	7.8	0.79	0.50	0.07		34.0	
11	601T4	200	7.8	0.74	0.53	0.10		34.1	
12	601T4	200	9.5	0.90	0.59	0.07		35.5	
13	601T4	250	7.8	0.62	0.54	0.07		32.2	
14	601T4	250	9.3	0.97	0.36	0.15		38.6	$\epsilon_{fail}=0.50\%$
15	601T4	250	11.3	0.79	0.60	0.10		39.0	$E_c=13.5\times10^6$psi
16	601T4	250	12.8	0.53	0.65	0.07		42.4	
17	601T4	250	14.5	0.78	0.52	0.07		45.1	
18	601T4	250	14.5	0.63	0.47	0.04		46.5	
19	601T4	300	9.5	0.76	0.48	0.07		36.8	
20	601T4	300	17.0	0.81	0.38	0.06		45.8	
21	201T6	0	0	0.45	0.44	1.24		58.5	$\sigma_{0.6}=49\times10^3$psi
22	201T6	0	0	0.41	0.40	1.33		62.5	$\sigma_{0.6}=47\times10^3$psi
23	201T6	0	0	0.58	0.49	1.22		60.5	
24	201T6	130	6.4	0.47	0.69	1.12		64.7	
25	201T6	150	8.2	0.63	0.66	1.15		69.5	
26	201T6	150	7.4	0.34	0.60	1.39		66.9	
27	201T6	250	8.6	0.40	0.37	1.08		66.8	
28	201T6	250	10.0	0.45	0.53	1.04		70.1	
29	201T6	250	12.1	0.28	0.42	1.38		68.8	$\epsilon_{fail}=0.63\%$
30	201T6	250	14.1	0.42	0.36	0.85		66.4	$E_c=15.3\times10^6$psi
31	201T6	250	17.0	0.50	0.55	1.26		63.2	
32	7178T6	0	0	1.06	0.77	2.19		70.4	$\sigma_{0.6}=56\times10^3$psi
33	7178T6	0	0	2.79	0.45	2.62		78.2	$\sigma_{0.6}=56\times10^3$psi
34	7178T6	0	0	1.49	0.86	3.39		72.0	$\sigma_{0.6}=56\times10^3$psi
35	7178T6	0	0	1.06	0.77	3.81		77.5	$\sigma_{0.6}=56\times10^3$psi
36	7178T6	250	9.6	2.31	0.39	2.14		68.5	
37	7178T6	250	12.8	2.62	0.53	2.22		78.1	
38	7178T6	250	13.8	2.38	0.40	2.35		75.7	
39	7178T6	250B*	10.0	1.31	0.88	3.53		83.6	
40	7178T6	250B*	12.7	1.08	1.00	3.63		83.8	
41	7178T6	250B*	16.4	1.47	1.00	3.69		88.6	
42	7178T6	250B*	19.0	2.16	0.44	3.74		88.6	

(*B: Bundle Structure)

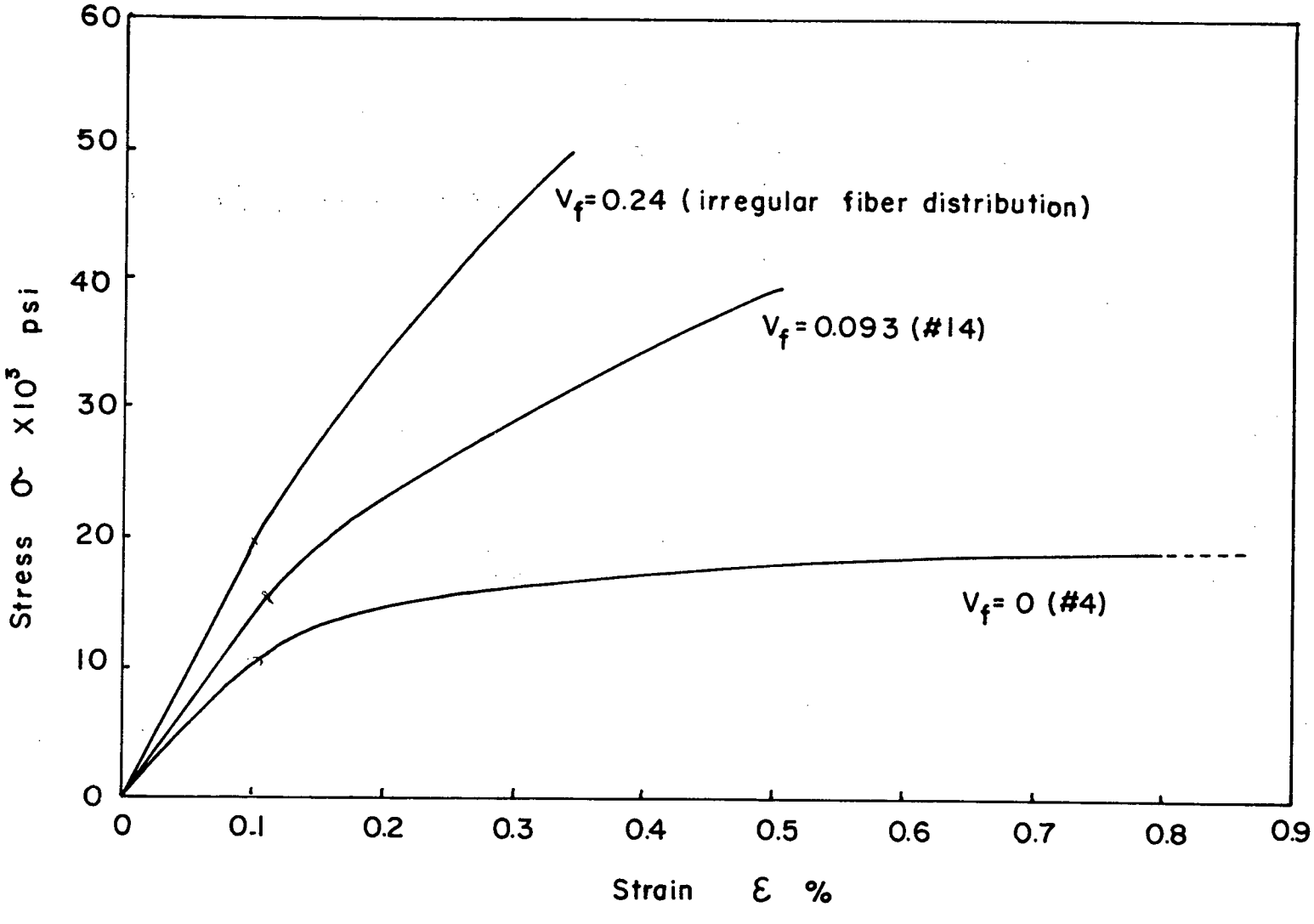

Fig.17. Stress Strain Curves of 601T4 Alloy and the Composites

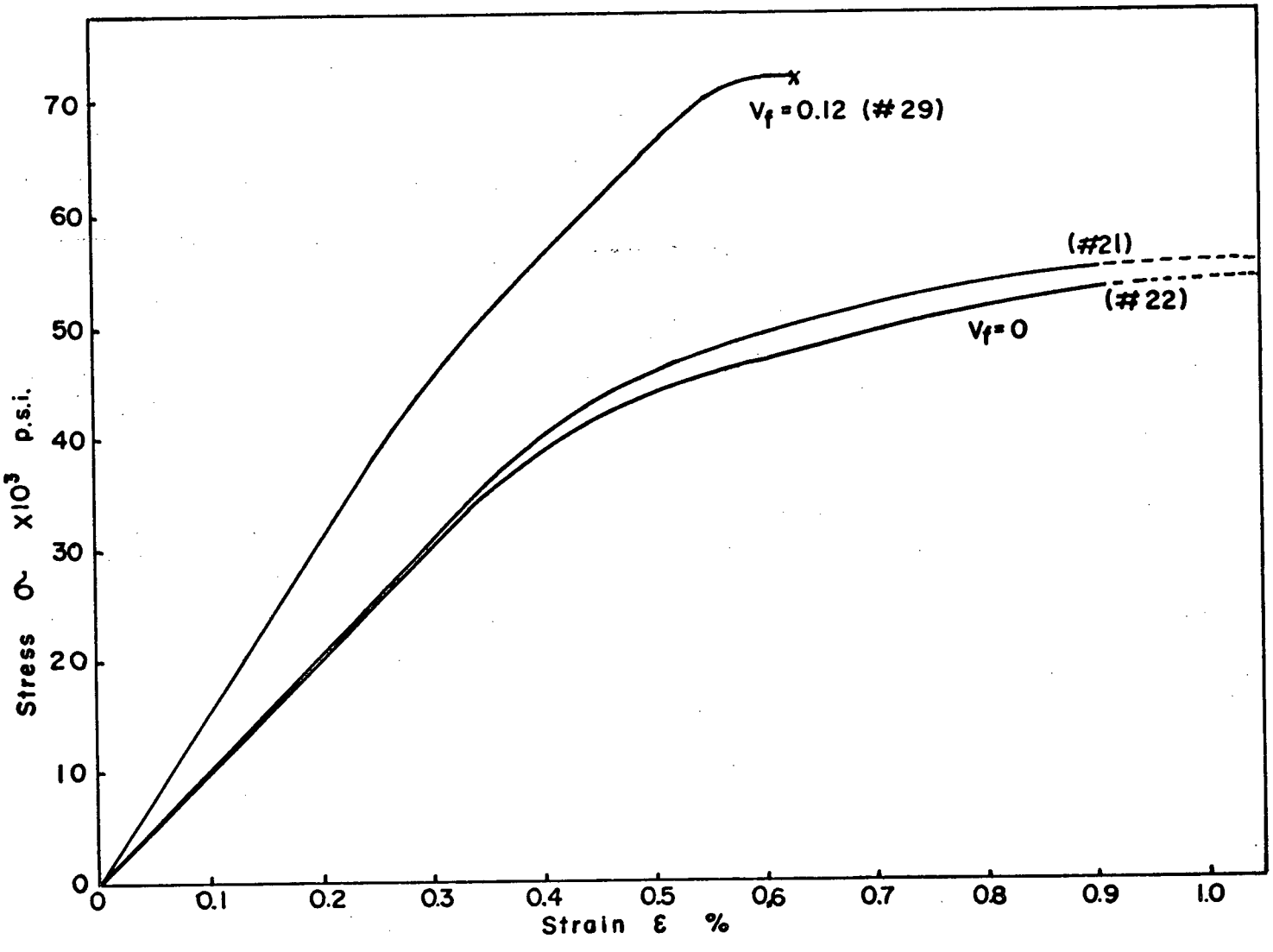

Fig.18. Stress Strain Curves of 201T6 Alloy and the Composite

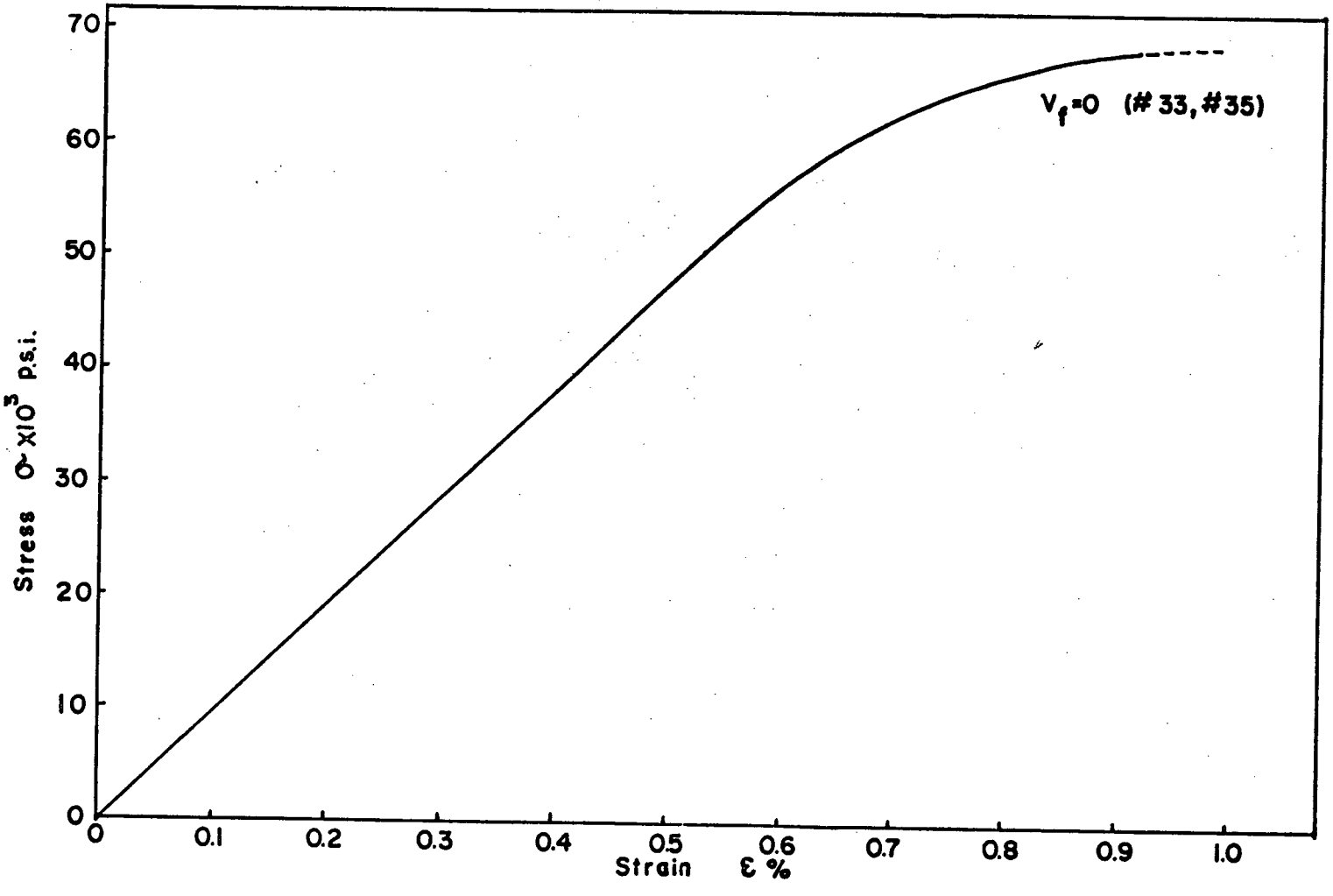

Fig.19. Stress Strain Curve of 7178 T6 Alloy

Table 9. Allowable Limits of the Matrix Composition

Alloy	Mg, at %	Si, at %	Cu, at %	Zn, at %
601	0.50-1.05	0.40-0.60	0.04 - 0.14	-
201	0.20-0.60	0.30-0.70	1.00 - 1.40	
7178	2.80-1.00	-	0.35 - 1.00	2.10-3.90

The measured strain of composite specimens was always small (0.06%). The Young's modulus of composite specimens derived from these stress strain curves are shown in Table 8. These values are in good agreement with the calculated values according to "rule of mixture".

Some of these stress strain curves are shown in Fig. 17, 18, and 19. The stress strain curve of 7178 T6 composite was not obtained because of the shortage of specimens due to the difficulty of controlling alloy composition.

III-4. Ultimate Tensile Strength

The variations in ultimate tensile strength, σ_c, of each alloy composites with fiber volume fraction, V_f, are shown in Fig. 20, 21, and 22. The ultimate tensile strength of unreinforced, blank, specimens, σ_{muts}, and the strength of the alloy at the breaking strain of the fibers, σ_m^*, are also plotted in these figures as the points corresponding to zero fiber volume fraction.

The ultimate tensile strength of non-uniform, bundle structure, 7178 T6 alloy composites is also shown in Fig. 22 to be compared with uniformly

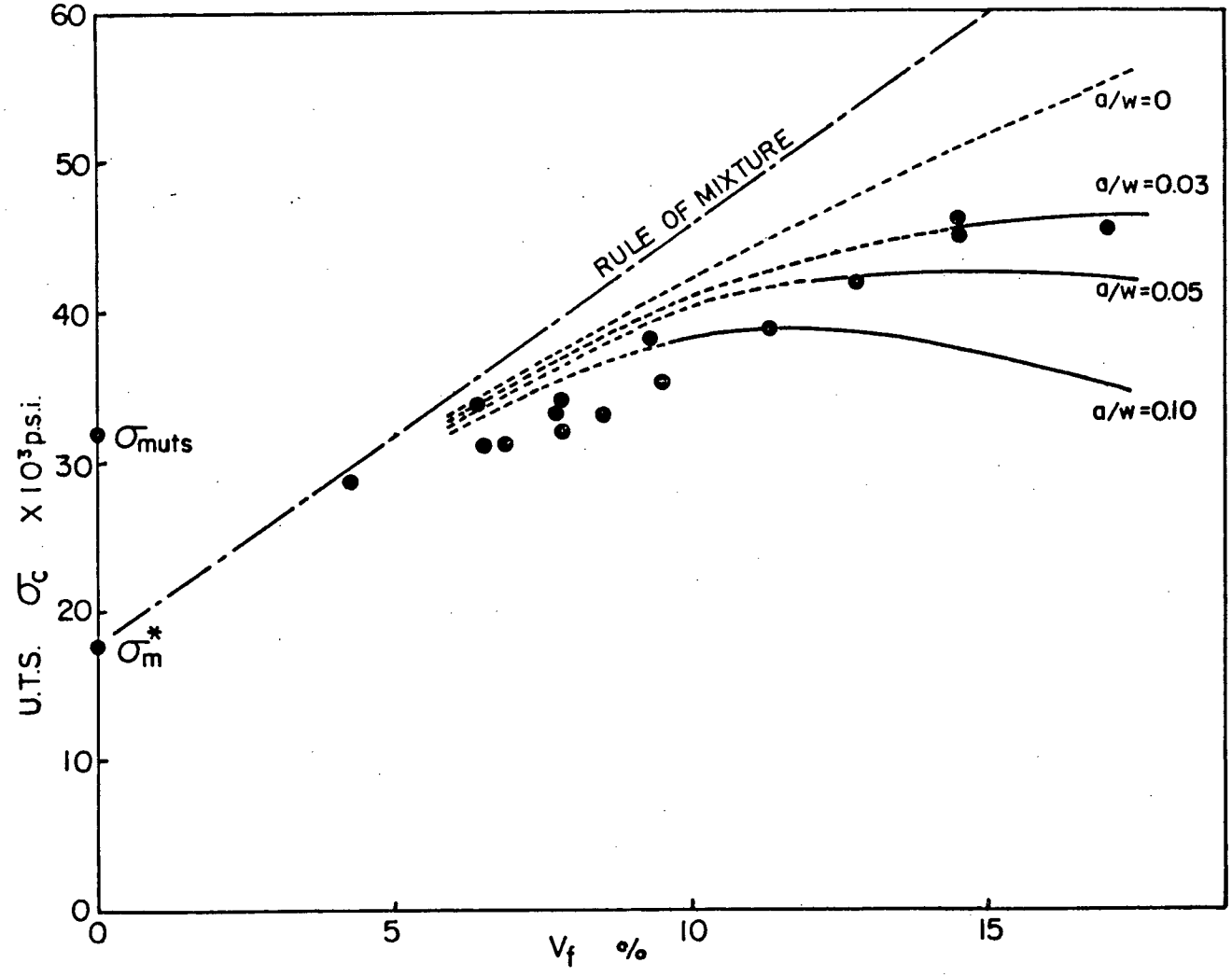

Fig.20. Tensile Strength of 6061T4 Composites, and Theoretical Curves

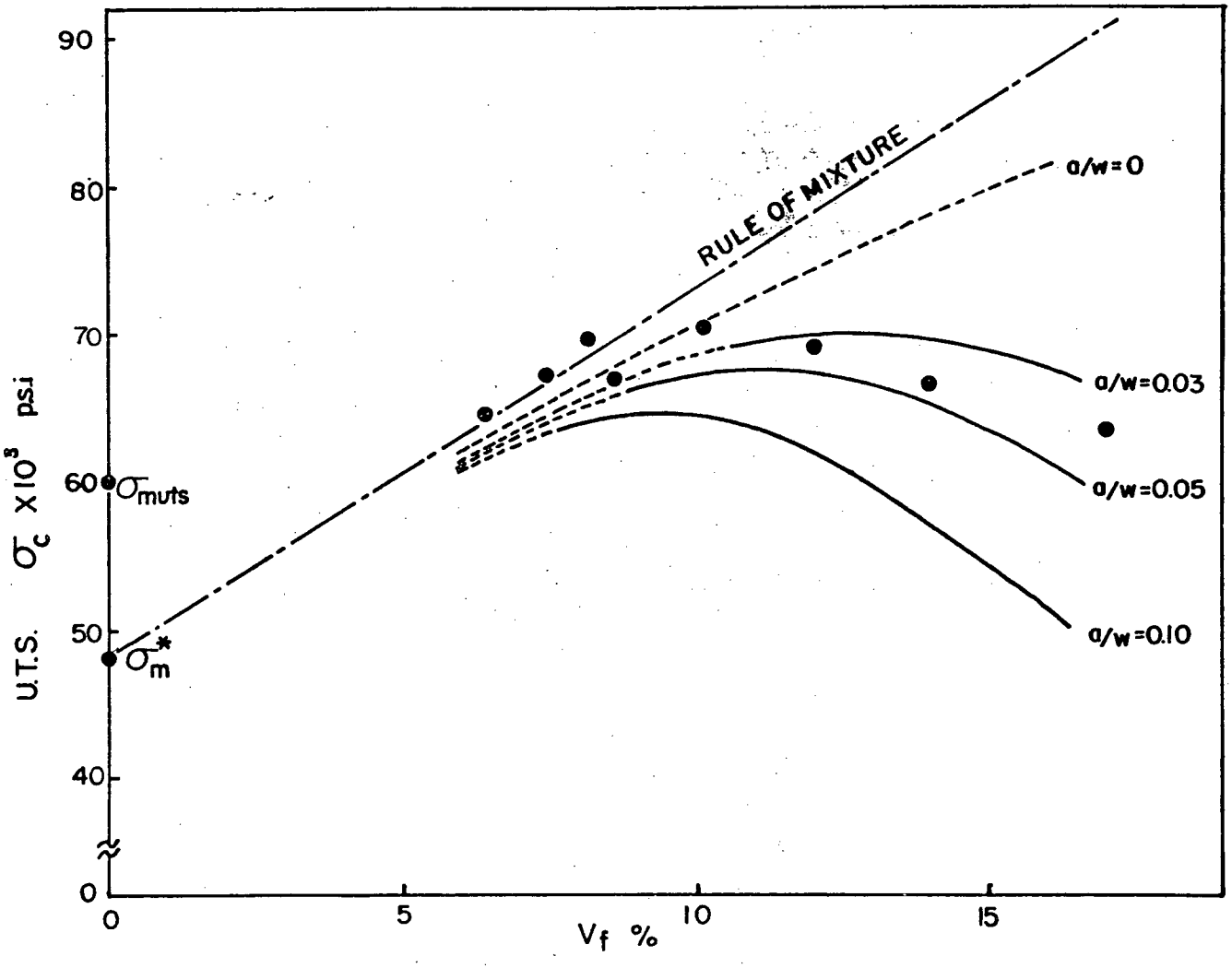

Fig.21. Tensile Strength of 201T6 Composites, and Theoretical Curves

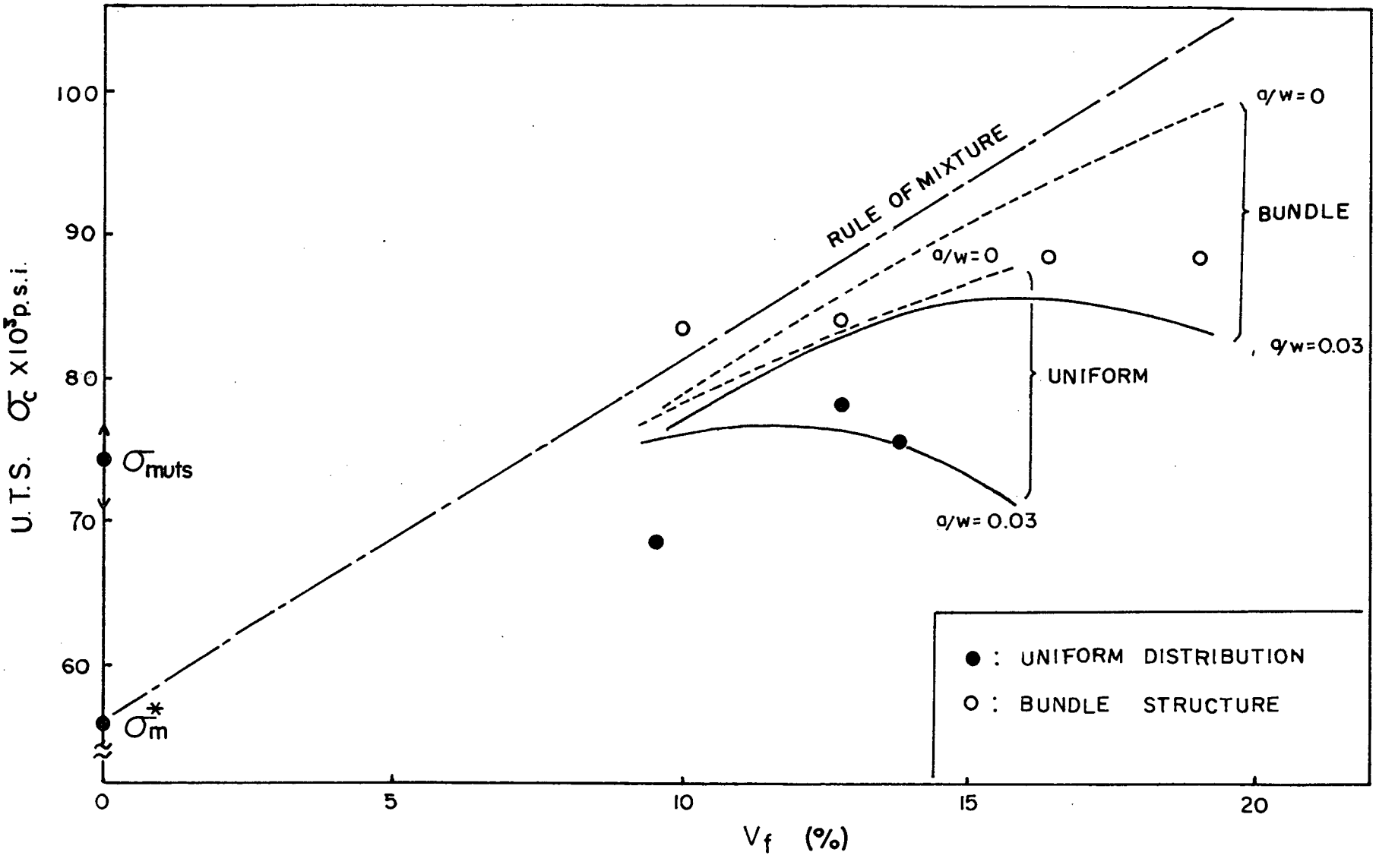

Fig.22. Tensile Strength of 7178 T6, Uniform and Bundle Structure Composites, and Theoretical Curves

distributed composites. The ultimate tensile strength of each composite calculated according to "rule of mixture" is also exhibited in these figures as a dot-dash line.

In all cases, the experimental values are lower than the "rule of mixture" level. The discrepancy between the experimental and the "rule of mixture" values becomes more evident as the fiber volume fraction increases. This tendency is more prominent in 201T6 composites than 601T4 composites.

The tensile strength of the bundle structure 7178 T6 composites is higher than the uniform composites as shown in Fig. 22. This result suggests that some other mechanism, which is different from the "rule of mixture", is operating to keep the strength of bundle structure composites higher than the uniform ones.

Other curves calculated according to a model which will be discussed later are also shown in these figures.

III-5. Fracture Elongation

An attempt was made to obtain the fracture elongation of specimens by measuring the distance between gauge marks on fractured specimen; however, the results were unreliable because of the difficulty in measuring very small elongations and also because of the frequent failure at specimen shoulders outside of the marks. Finally, the measurement by this method was abandoned. Only a few data about the elongation of these composite specimens are available from the strain gauge test data as shown in Table 8.

III-6. Microscope Observations of Tested Specimens

Fractographic observations were made using a scanning electron microscope. The plastic deformation of the matrix at the fracture surface is prominent. A small amount of fiber pull out was usually observed. Small voids, which are characteristic of plastic failure, were observed somewhere on the ridges of the matrix as shown in Fig. 23 and Fig. 24.

The fiber failure zone which appeared on the polished 201T6 composite specimen surface was observed using optical and scanning electron microscopy, after straining close to the fracture point. The typical appearance of the zone surface is shown in Fig. 25. Within the zone, fibers were broken into small fragments as shown in the scanning electron micrograph at low magnification (x200), Fig. 26. The slip lines are observed at a higher magnification (x 1000) in the grains between fibers as shown in Fig. 27.

The interior structure of this specimen was examined by further polishing and etching. A fiber failure region around a specimen shoulder is shown as a marked area in Fig. 28. In this figure, the successive propagation of fiber failure from the right hand side to the left hand side seems to be interrupted at a fiber free (or low fiber density) region. Etched grain boundaries, and broken and slightly tilted fibers were also observed as shown in Fig.29.

Fractured fibers can be seen at a considerably longer distance from the fracture surface in the low V_f composite (Fig. 30a) than in the high V_f composite (Fig. 30b). This same tendency is also observed in the case of 201T6 composites of different V_f values, 6.4% and 17% as shown in Fig. 31 (a) and (b).

The broken fragments located closer to the fracture surface have generally shorter lengths than the fragments located at a larger distance

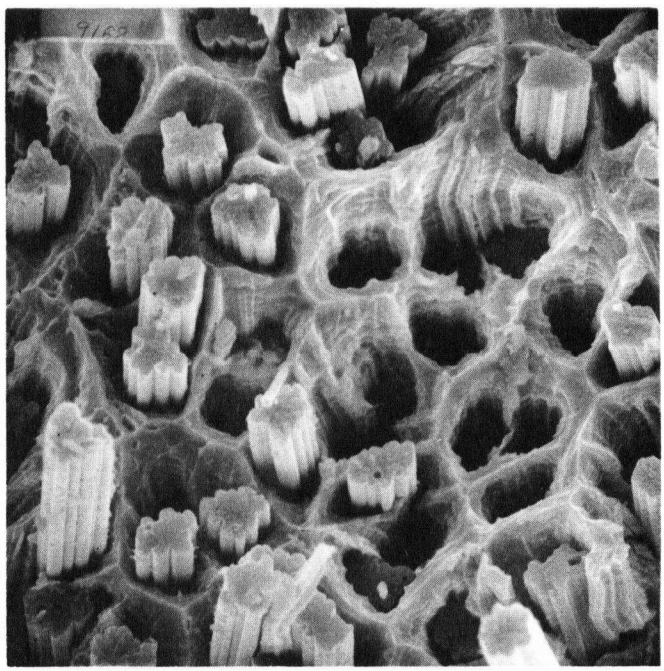

Fig.23. Fractured Surface of 6061T4 Composite, #17, 14.5% V_f, x 1000.

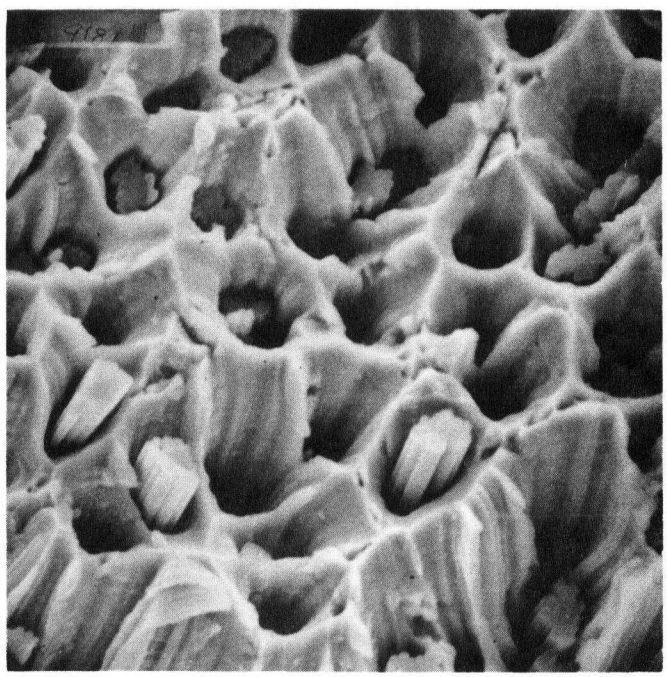

Fig.24. Fractured Surface of 2017T6 Composite, #29, 12.1% V_f, x 1000.

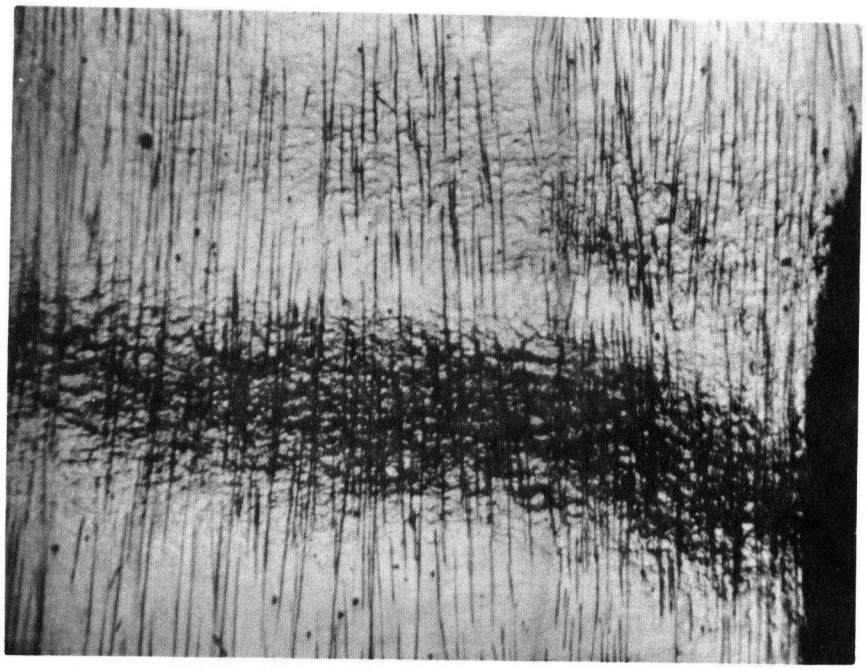

Fig.25. Fiber Failure Zone near Specimen Shoulder Polished Surface of a 201T6 Composite Specimen, x 32.

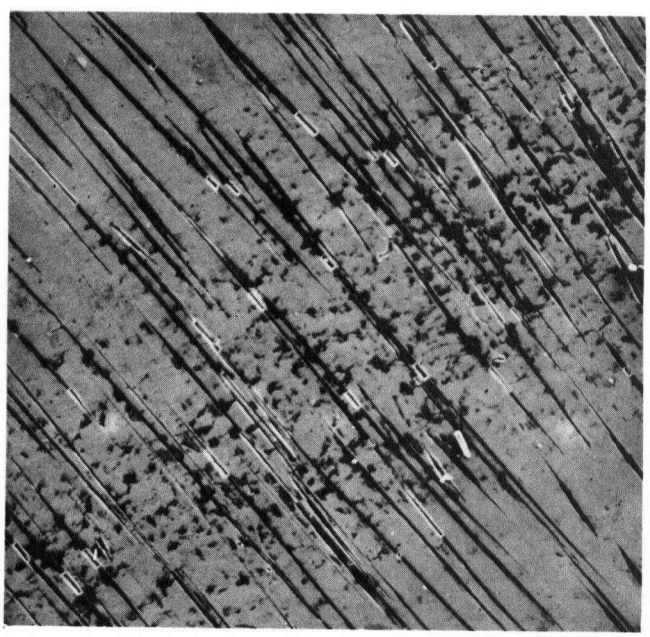

Fig.26. Scanning Electron Micrograph of Fiber Failure Zone Surface Showing Broken Fibers, x 200.

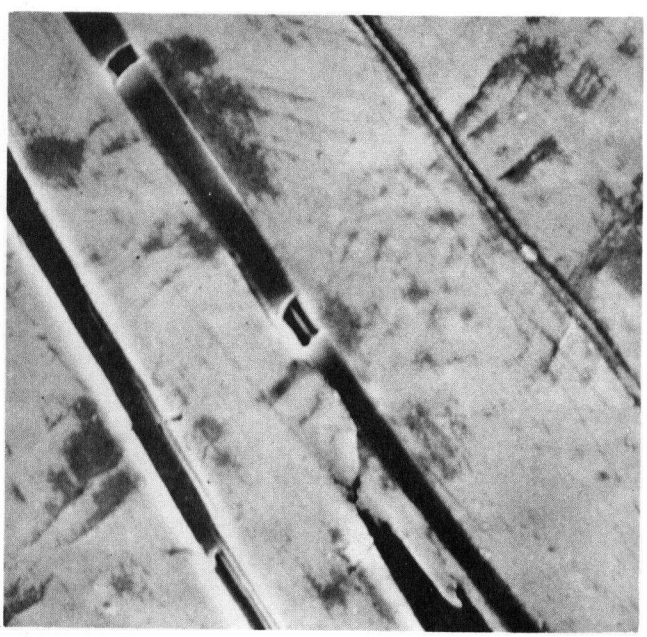

Fig.27. Scanning Electron Micrograph of Zone Surface Showing Slip Lines, x 1000.

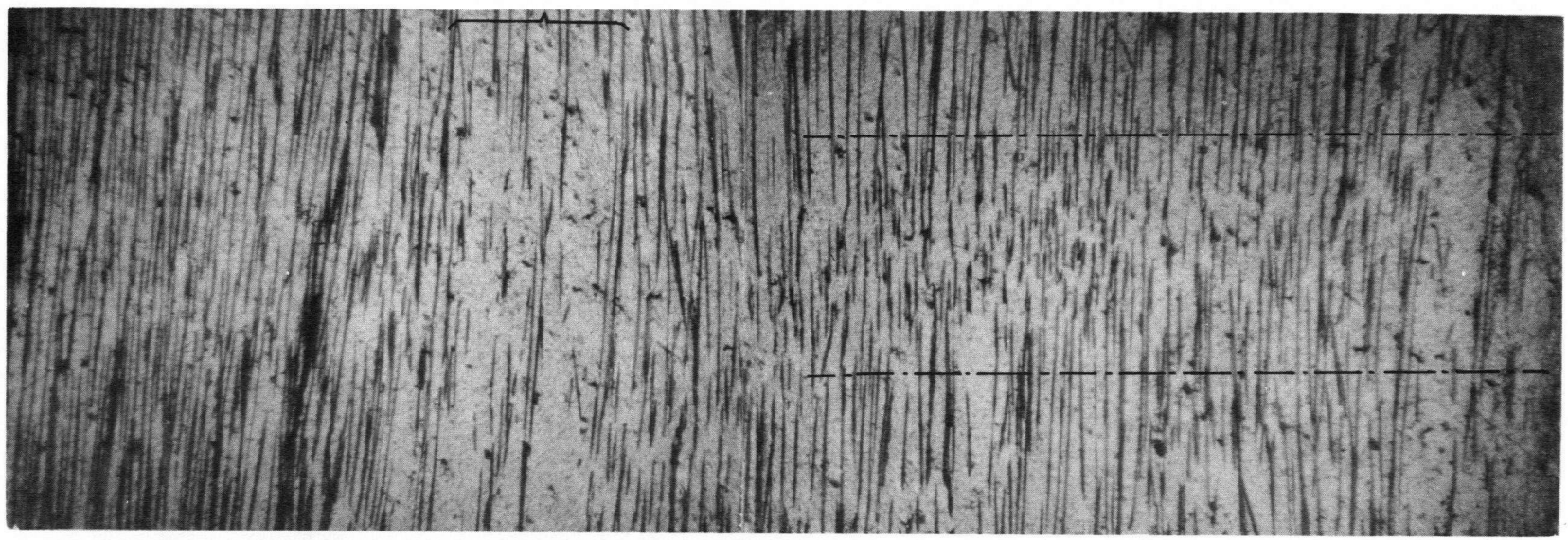

Fig.28. Micrograph Indicating Propagation of the Fiber Failure prior to Failure of the Specimen, Longitudinal Section, x 32.

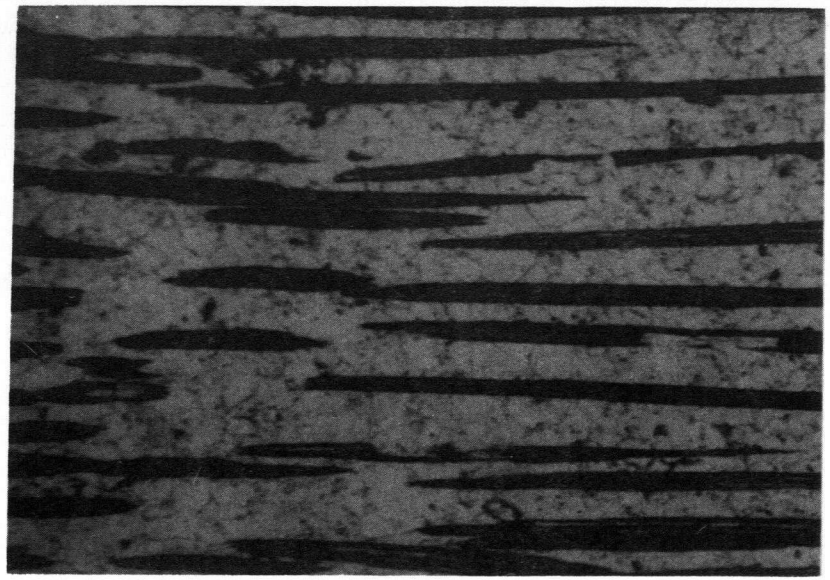

Fig.29. Longitudinal Section around the Zone Showing Matrix Grains, and Broken Tilted Fibers, NaOH Solution Etch, x 180.

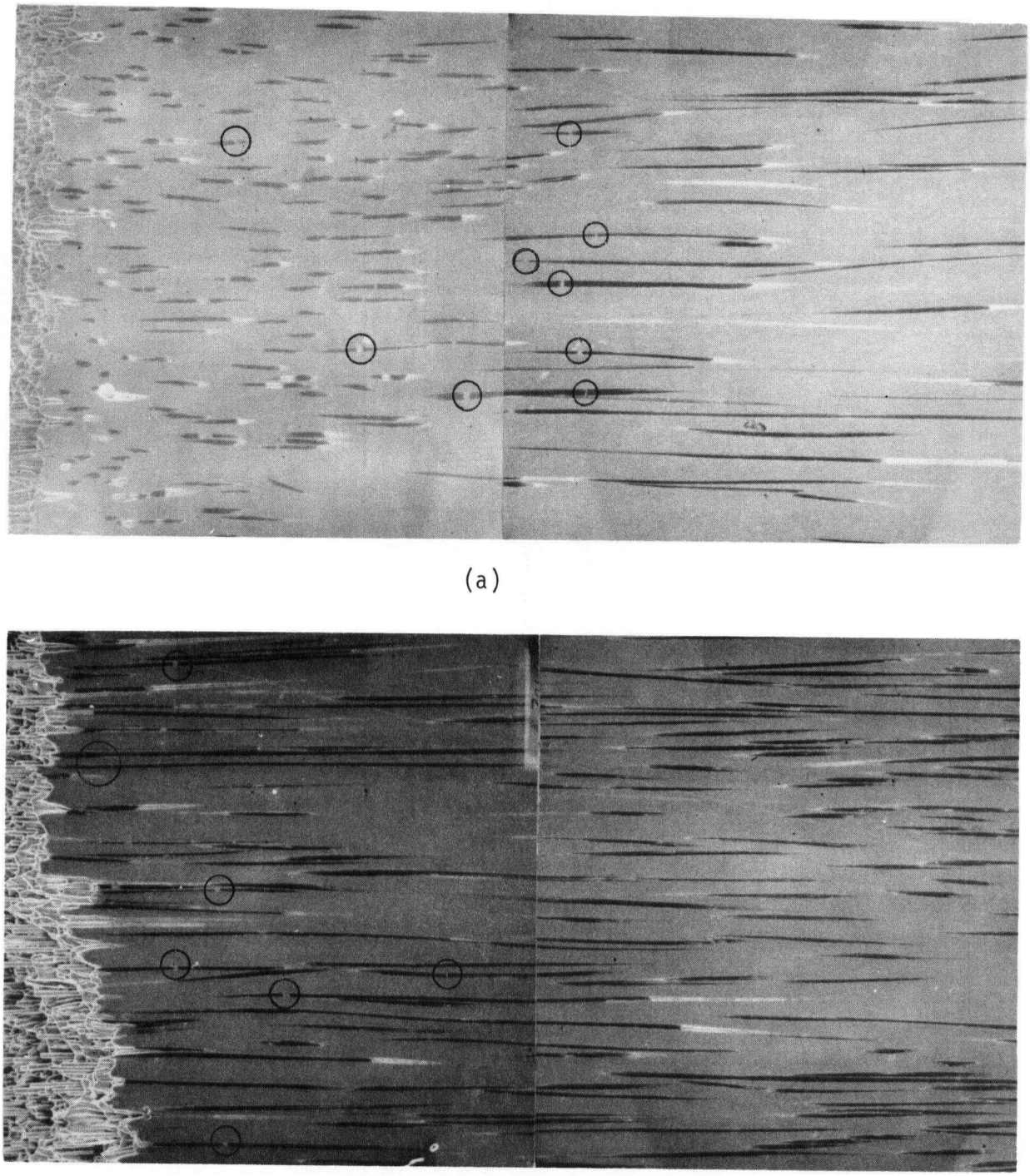

Fig.30. Longitudinal Sections of Fractured 601T4 Specimens, Showing the Difference in the Distribution of the Fracture Points in(a)Low V_f (8.5%), #9, and(b)High V_f (14.5%), #17, Composites, Small Circles Showing Fractured Fibers, x 100.

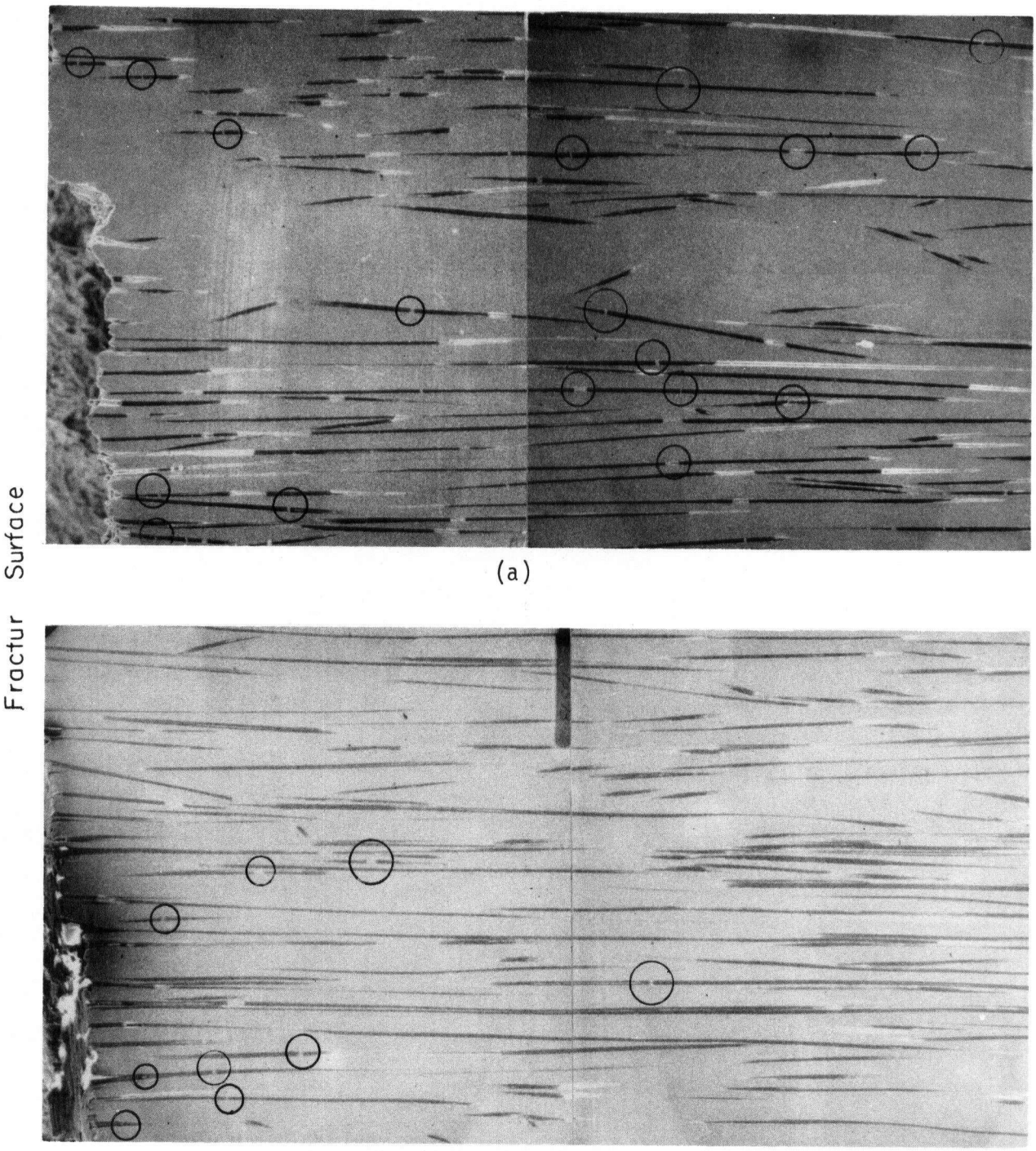

Fig.31. Longitudinal Sections of Fractured 201T6 Specimens Showing the Difference in the Distribution of the Fractured Points in a Low V_f (6.4%), #24, and(b)High V_f (17%), #29, Composites, Small Circles Showing Fractured Fibers, x 100.

from the fracture surface, as shown in these pictures.

Scanning electron micrographs at low magnification (x50) were used to quantify the fiber failure zone thickness. The quantitative measurements were made of the distance, B_f, from the fracture surface to the furthest point at which broken fiber fragments could be observed. The results are given in Table 10. The relation between B_f and the fiber volume fraction, V_f, and Young's modulus E_c was examined and this is discussed in a later section IV-2-iv. Fig. 32 shows the variations of B_f values with these factors.

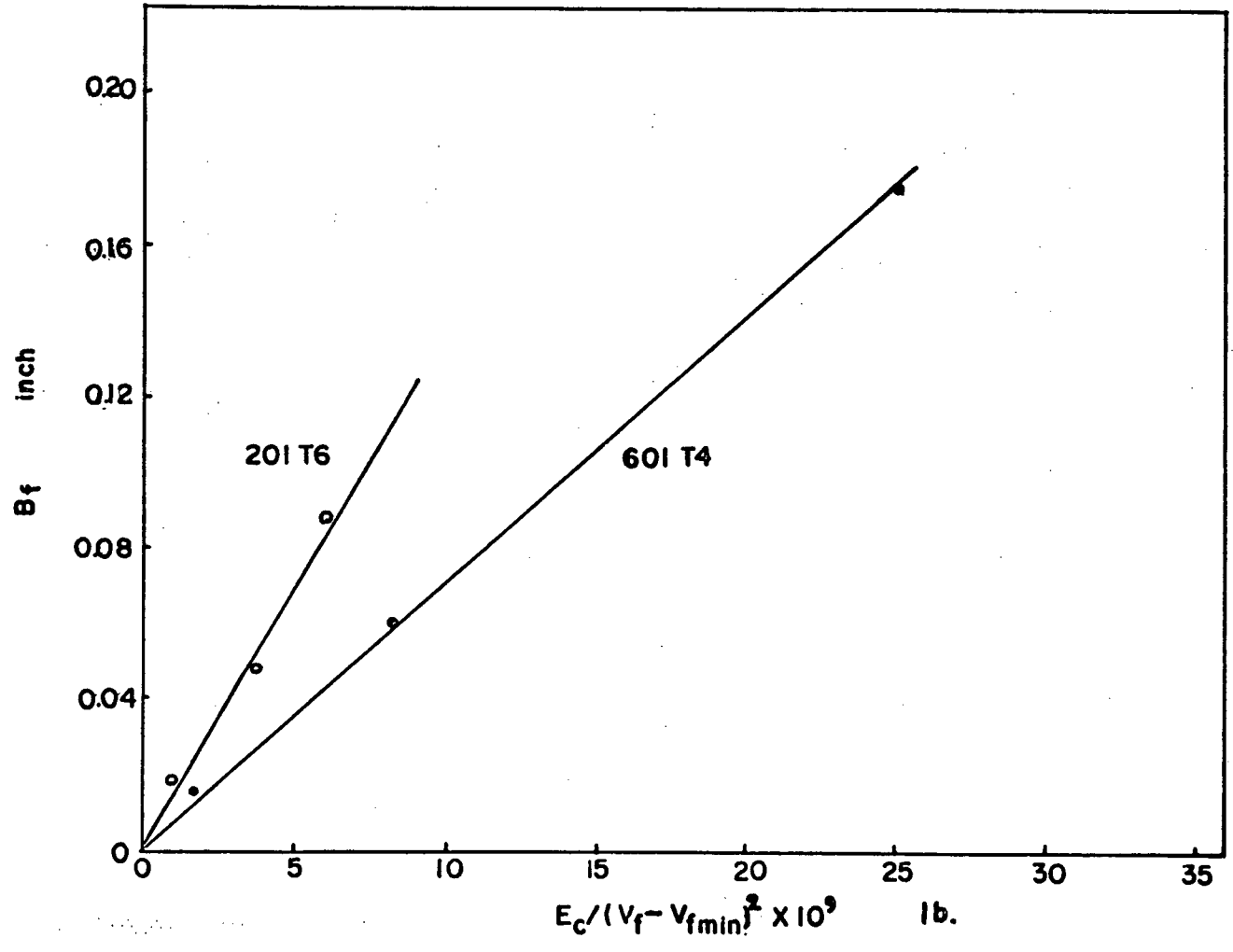

Fig.32. Relation between B_f, E_c, and V_f

Table 10. Data for Fiber Fracture Zone Characteristics

Alloy	$\frac{V_{fmin}}{\sigma_{muts} - \sigma_m^*}$ / $\sigma_{futs}+\sigma_{muts}-\sigma_m^*$	V_f	$V_f - V_{fmin}$	$E_c \times 10^6$ psi $(E_f V_f + E_m V_m)$	$E_c \times 10^9$ psi $(V_f - V_{fmin})^2$	B_f inch
601T4	0.0446	0.067	0.0224	12.68	25.3	0.17
		0.085	0.0404	13.40	8.21	0.06
		0.145	0.1004	15.80	1.57	0.02
201T6	0.0385	0.086	0.0475	13.44	5.96	0.09
		0.10	0.0615	14.00	3.70	0.05
		0.17	0.1315	16.80	0.972	0.02

IV DISCUSSION

IV-1. Rule of Mixture

IV-1-i. Rule of Mixture for Continuous Fiber Reinforced Materials

Since Kelly and Tyson (41) proposed the so called "rule of mixture" for the strength of composites, it has been quite often used to evaluate the composite strength. In this rule, the stress on the composite specimen σ is expressed as the summation of stresses which both fibers and the matrix are supporting at the same amount of strain as shown in Fig. 33. This relation can be obtained by assuming the same strain in fibers and the matrix.

$$\sigma = V_f \sigma_f + V_m \sigma_m \qquad (1)$$

Where, σ : stress in a composite at a certain strain

σ_f : stress in fibers at the same strain

σ_m : stress in matrix at the same strain

V_f : fiber volume fraction

V_m : matrix volume fraction (= $1-V_f$)

Dividing eqn. 1 by a strain, ϵ , which is smaller than the yield strain of the matrix ϵ_y, the rule of mixture for Young's modulus of the composite, E_c is obtained

$$E_c = \sigma/\epsilon = V_f \sigma_f/\epsilon + V_m \sigma_m/\epsilon \qquad (2)$$

$$\text{i.e.} \quad E_c = V_f E_f + V_m E_m \qquad (3)$$

where, E_f = Young's modulus of fibers

E_m = Young's modulus of the matrix

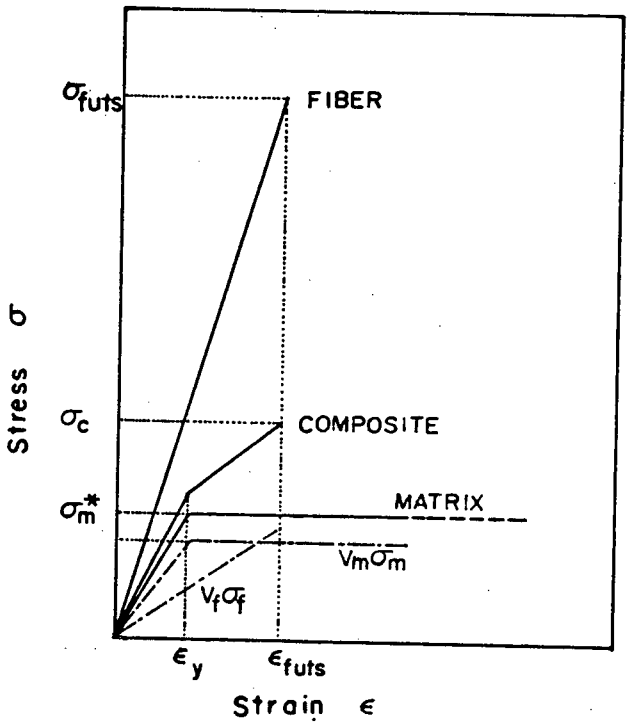

Fig.33. Schematic Diagram of Stress Strain Curves of the Composite, the Fiber, and the Matrix, obtained according to "Rule of Mixture"

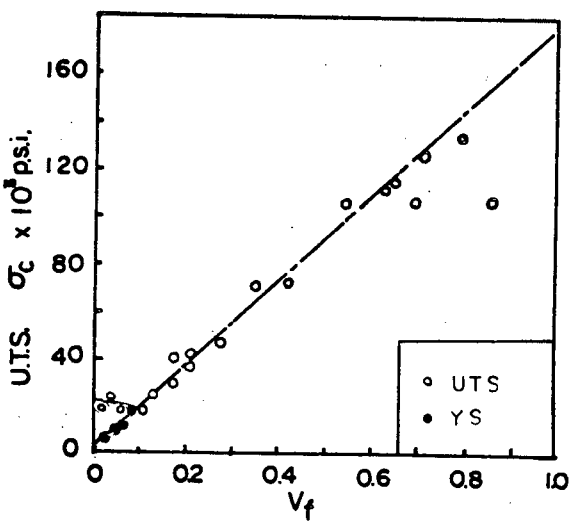

Fig.34. Tensile Strength of Copper Reinforced with 5 mm Continuous Brittle Tungsten Wires (41).

If it is assumed that all the fibers fail at the same time when they reach the failure strain, the failure stress σ_c can satisfy the "rule of mixture" condition. Consequently, the strength of the composite, σ_c, is given in the following expression as "rule of mixture" for the composite strength.

$$\sigma_c = V_f \sigma_{futs} + V_m \sigma_m^* \qquad (4)$$

where, σ_{futs} : tensile strength of fibers

σ_m^* : flow stress of the matrix at the same strain with fiber fracture.

In the present work, the strength values calculated according to this equation have been discussed.

When the volume fraction of fibers is less than V_{crit}, fibers are thought to be broken successively, i.e. one after another, before the matrix fails. The maximum strength of such a composite is expressed in the following equation, because only the matrix is thought to support the load at the failure point.

$$\sigma_c = \sigma_{muts} (1 - V_f) \qquad (5)$$

where, σ_{muts} : tensile strength of the matrix

The critical fiber volume fraction, above which the "rule of mixture" condition is satisfied (if overall fiber fracture occurs), is obtained from Eqn. 4 and 5.

$$V_{fcrit} = (\sigma_m - \sigma_m^*)/(\sigma_f - \sigma_m - \sigma_m^*) \qquad (6)$$

Furthermore, the fiber volume fraction has to exceed some value V_{min} to strengthen the composite. This value is obtained by substituting

the σ_c in Eqn. 4 with σ_{muts}.

$$V_{min} = (\sigma_m - \sigma_m^*)/(\sigma_{futs} - \sigma_m^*) \quad (7)$$

Fig. 34 shows experimental data which were obtained by Kelly and Tyson to prove "rule of mixture" for the strength of Cu-W wire composites.

IV-1-ii. Strength of Discontinuous Fiber Reinforced Materials

In the case of discontinuous fibers, the load on a composite is thought to be transferred to the fibers through the matrix. The strength of a discontinuous fiber composite becomes close to the strength of a continuous fiber composite as the aspect ratio, ℓ/d , (the ratio of fiber length and diameter) increases.

There are three theoretical works which can be distinguished from each other only by the difference of assumptions about the elasticity or the plasticity of the matrix (42, 43). In this section, only Kelly-Tyson's theory (91) is described which is based on the assumption of elastic fibers and the plastic matrix, because this assumption is mostly applicable in the case of metal matrix composites.

Now consider the case where the matrix is allowed to flow plastically. When a composite of discontinuous fibers is stressed in a direction along the fiber axis, different axial displacements take place in the matrix and fibers, and a large shear stress occurs at the end of the fibers. Fig. 35 is a model of a single discontinuous fiber in the cylindrical matrix. The load is transferred from the matrix to the fiber only by the shear stress at the interface, τ_{rz} , neglecting any stress transfer across the fiber ends which have small area. The small increment of the load,

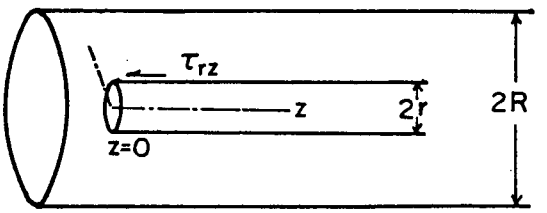

Fig.35. Showing Notation Used in the Kelly and Tyson's Theory for the Discontinuous Fiber Composites (41).

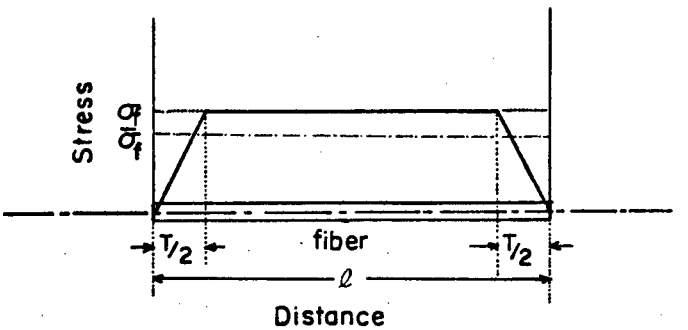

Fig.36. Expected Variation of Stress along a Fiber within a Plastic Metal Matrix (41).

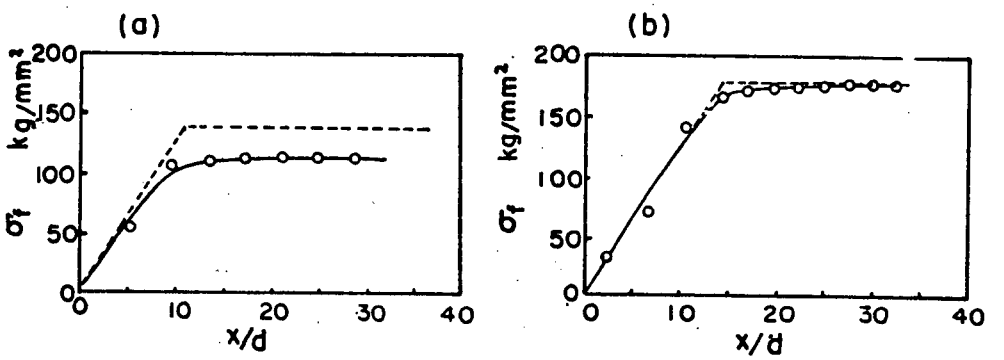

Fig.37. Stress Distribution in the Discontinuous Tungsten Fiber Obtained by Means of Moiré Technique. Applied Stress on the Composite is Low (a) and High (b) (44) (47). (x: distance from one end of the fiber, d: diameter)

dP, due to the stress transfer at the small interface area $2\pi r_o dz$ is given by

$$dP = 2\pi r_o \tau_{rz} dz \tag{8}$$

Equation 8 integrates to

$$P = 2\pi r z \tau \tag{9}$$

For a plastic matrix which does not work-harden, τ is constant. If the interface fails, τ is equal to the frictional force per unit area which the matrix exerts on the fiber as it slides over the fiber. For work-hardening matrix, τ depends on the strain in the composite and is thought to be identified with the ultimate shear strength of the matrix.

Eqn. 9 means that the stress in a fiber builds up linearly from both ends as shown in Fig. 36. The stress in the fiber at a distance z from the end, σ_{zz}, is expressed by

$$\sigma_{zz} = \frac{P}{\pi r^2} \tag{10}$$

substituting for P from Eqn. 9,

$$\sigma_{zz} = \frac{2\tau z}{r} \tag{11}$$

The strain in the fiber cannot exceed the strain of the matrix so that σ_{zz} will build up to the value σ_f, provided the fiber is sufficiently long. If the stress in the fiber, σ_{zz}, builds up to the fracture stress of the fiber σ_{futs}, the fiber is broken. The critical fiber length, T, for this to take place is given by

$$T = r\sigma_{futs}/\tau \tag{12}$$

T/2 is defined as the transfer length. The value of T depends on τ. If τ is constant as in the case of a non-work hardening matrix, T is also constant.

If a condition of fiber length, ℓ, > T, is satisfied, the fracture of the composite occurs when σ_f increases to the ultimate tensile strength of the fiber, σ_{futs}. The average tensile stress, $\bar{\sigma}_f$ at this loading point is expressed as follows

$$\bar{\sigma}_f = \frac{1}{\ell} \int_0^{\ell} \sigma_{zz} dz$$

$$= \sigma_{futs}\left(1 - \frac{T}{2\ell}\right) \qquad (13)$$

An equation which expresses the tensile strength of the discontinous fiber composites is obtained, treating $\bar{\sigma}_f$ as the stress in the fibers in continuous fiber composites. From Eqn. 4 and 13,

$$\sigma_c = \sigma_{futs}\, V_f\, (1 - T/2\ell) + \sigma_m^*\, V_m \qquad (14)$$

It is seen from this equation that the strength of a discontinuous fiber composite becomes closer to the strength of continuous ones if the fiber length, ℓ, is much greater than the transfer length, T/2.

Miura and Okuno's (44) study on the stress distribution of a two-dimensional Al-W wire composite by means of the Moiré technique proved the appropriateness of the stress distribution in fibers in this model. Their results are shown in Fig. 37.

T, τ, and $\bar{\sigma}_f$ are used as important variables later in the following discussions. The Equation 14 is used to express the strength of the fiber failure zone.

IV-2. Propagative Fiber Failure Model for Graphite Fiber Reinforced Aluminum Alloy Composites

IV-2-i. Ultimate Tensile Strength of Homogeneously Distributed Specimens

The composite tensile specimens of 601 T4 (solution treated), 201 T6 (age hardened) and 7178 T6 (age hardened) alloys exhibited great discrepancy between experimental strength values and values calculated according to "rule of mixture" as shown in Fig. 20, 21, and 22. The experimental U.T.S. values of 601 T4 and 201 T6 alloy composites against fiber volume fractions appear to be on broad curves in spite of great scattering.

The scatter of strength values in these experimental results might be due to:

a) misorientation of the fibers with the specimen axis. The fibers might not be aligned properly during the infiltration-sedimentation process, especially in the case of low fiber volume fraction composites.

b) non-uniform fiber distribution in the matrix and the contacts of neighboring fibers which may act as defects.

c) deviations of matrix chemical composition from average values. The ultimate tensile strength of the matrix is dependent on its chemical composition. The great density difference of each alloy element might cause great difference of settling speed among the powders of each element in the infiltration-sedimentation process.

d) error in the measurement of fiber volume fractions. The micrographs which cover only one-seventh of the total specimen section were used to count the numbers of fibers, so that error of a few percent is unavoidable.

No quantitative measurements were done to estimate the contributions to the scatter from each one of the above factors.

General microscope observation revealed that the breakage of graphite fibers occurs in a narrow region close to the fracture edge of the specimens; however, the fibers' failure is in a brittle manner and the matrix failure is in a ductile manner as expected from the original deformation characteristics of each material.

This result suggests that most of the plastic deformation of the matrix takes place in a limited range from the fracture surface, where fibers are broken. The propagation of a rather highly strained deformation zone was observed in specimens being strained to some extent before the failure as shown in Fig. 25. The segments of broken fibers were also observed in this zone as shown in Fig. 26, etc. The strain of the matrix in this zone is higher than the matrix of the other part of the specimen as shown in Fig. 27.

From these results, it may be said that such a highly strained zone propagates over the section of the specimen, breaking the fiber successively at the tip front of the zone, during the tensile test. Such successive failure of fibers in the matrix has been observed in boron filament reinforced aluminum composites by J. Steele et al. (45). In the present work, the model proposed is one in which the ultimate tensile strength of the composites corresponds to the accelerated propagation of a fiber failure zone.

This failure mode of composites is quite different from the model which A. Kelly et al. adopted to establish "rule of mixture" for large diameter fiber metal composite like W wire-Cu composites. In the model for "rule of mixture", all the fibers in the composite are assumed to fail at

once or at an idealized condition. The discrepancy in the experimental strength values and "rule of mixture" values may be mainly due to the difference between the actual propagative failure mode and the idealized failure mode in "rule of mixture" model. The observed propagative failure mode is going to be discussed in mathematical expression in successive pages, in order to give a possible explanation for experimental results.

IV-2-ii. Energy Criteria of Propagative Fiber Failure for Homogeneously Distributed Composites.

It is assumed for simplicity that fibers always deform in an elastic manner and the matrix changes its deformation mode from elastic to plastic which does not include any work hardening effect when it is stressed beyond the yield point, σ_{my}, i.e. $\sigma_{my} = \sigma_m^*$ in Fig. 38.

As a simple illustration, consider a plate specimen of width w and unit thickness containing a small half elliptical zone in which the fibers have failed into small segments of average transfer length, T_{uts}. The zone length is expressed as half of the long diameter of an ellipse, a, and the thickness is also expressed as the short diameter, 2b, in Fig. 39. The strain of the matrix outside this half elliptic zone is expressed as ϵ_o and within this zone as the fiber failure strain ϵ_{futs}, ($\epsilon_{futs} > \epsilon_o$). The stress on fibers outside of this zone is expressed as σ_{fo}, which is lower than the maximum stress on the fiber fragments within this zone σ_{futs}. The average stress on the fragments is $\frac{1}{2}\sigma_{futs}$. The stress distribution on broken fiber segments in this zone is assumed as shown in Fig. 40. The stress is transferred from the matrix to the segment through a shear stress, τ, at the interface of matrix and fiber segments. The stress on the

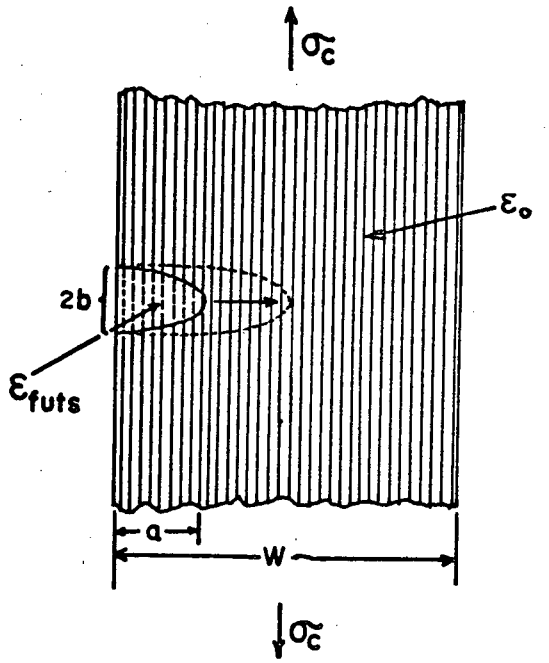

Fig.39. Half Elliptic Fiber Failure Zone in a Composite

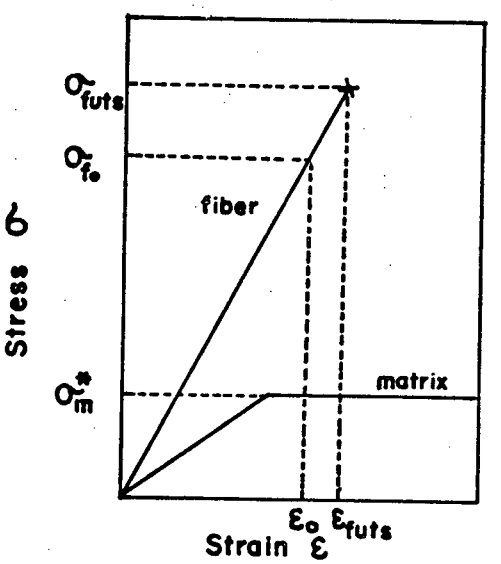

Fig.38. Schematic Diagram of Stress Strain Curve of the Matrix and the Fiber

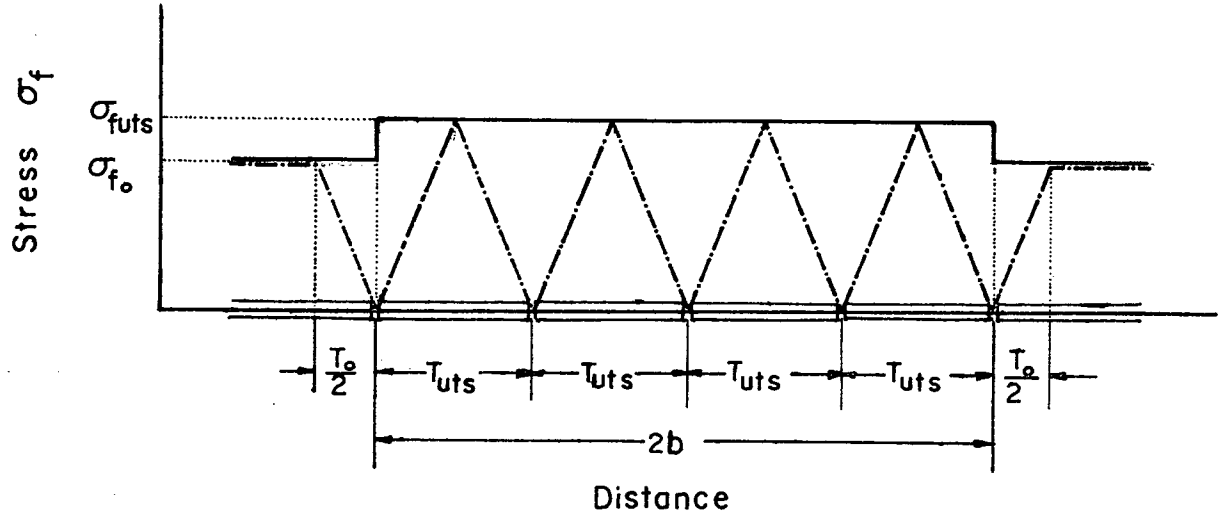

Fig.40. Stress Distribution Change in a Fiber which is Located in the Fiber Failure Zone. solid line: before failure, dot-dash-line: after failure.

fiber builds up linearly to the value σ_{futs} from the ends of the segments. For a plastic matrix which does not work-harden τ is constant.

$$\sigma_{futs} = \tau T_{uts} / r \qquad (15)$$

where r : radius of fibers

In other words, fibers are assumed to be broken into small segments which cannot be broken shorter than this by the further plastic deformation of the matrix.

The average stress in a segment in this zone, $\bar{\sigma}_{seg}$, is given in the following expression from Eqn. 13.

$$\bar{\sigma}_{seg} = \sigma_{futs} / 2 \qquad (16)$$

Consequently, the strength of this zone, σ_z, is obtained from Eqn. 14.

$$\sigma_z = \frac{1}{2} V_f \sigma_{futs} + V_m \sigma_m^* \qquad (17)$$

During a tensile test, such small half elliptic fiber failure zones first start to grow at some stress concentrated areas or defective areas in a specimen as shown in Fig. 41, deviating the actual stress-strain curve from a curve expected from "rule of mixture". Some amount of energy, dW_z, is required to grow a zone from the shape of a and b to a+da and b+db. During this growth, the load does work, $|dL|$. A change of elastic energy, dU, occurs in the region outside of the failure zone due to the shape change of the zone.

The elastic energy change may be easily understood if we consider the following special loading system shown in Fig. 42. Fig. 42(a) shows the specimen strained to the state of elongation $\Delta\ell$. The area $\square$ OYAC

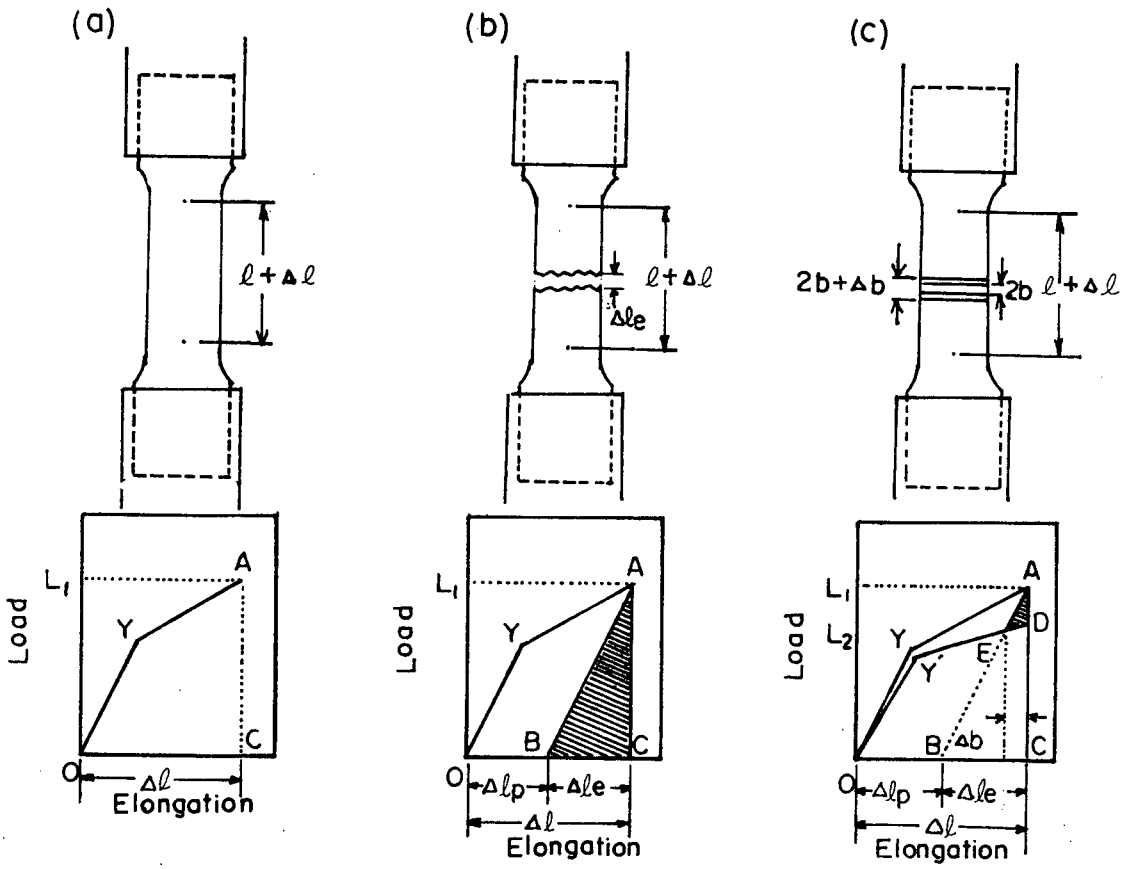

Fig.42. Schematic Curves for Model Development

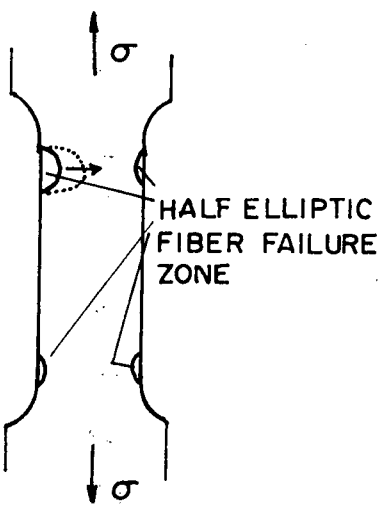

Fig.41. Fiber Failure Zones in a Specimen

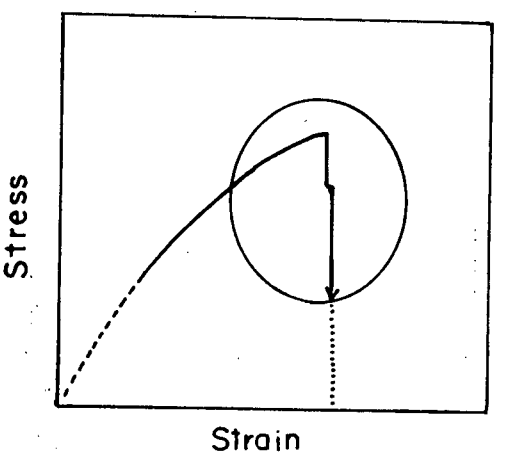

Fig.43. Schematic Diagram of Stress Strain Curve at Failure Point

corresponds to the work which the load did. If this specimen is broken under the condition of fixed grip distance, the two separated pieces shrink elastically and release elastic energy which corresponds to the hatched area $\triangle ABC$ shown in Fig. 42(b). If we strain a specimen, in which a fiber failure zone has traversed the cross section, to give the same amount of elongation, $\Delta \ell$, the load is increased following the stress-strain curve OY'ED in Fig. 42(c). Consequently, if we assume that the same fiber failure zone (which traversed the section) of thickness 2b, is formed in a specimen between fixed grips, the load is lowered from original, L_1 to the load, L_2, which corresponds to Eqn. 17. During this unloading under the fixed grip condition, the regions outside of the zone shrink elastically releasing energy which corresponds to the area $\triangle AED$ in Fig. 42(c). In the case of half elliptic fiber failure zone, some elastic energy which is a complicated function of the shape of the zone, a and 2b, is released from outside of the zone in the same way as the case of Fig. 42(c).

We let dW_t be the total free energy change of a specimen due to the formation of half elliptic fiber failure zone. Then dW_t is given by

$$dW_t = dL + dW_z + dU \tag{18}$$

When one of the zones grows up to a critical size, the summation of the potential energy change of the load, dL, and the elastic energy change, dU, can be big enough to supply the formation energy of the zone, dW_z. The energy balance at this critical point is given by

$$dW_t = dL + dW_z + dU = 0 \tag{19}$$

Once this relation is satisfied, the zone can start to grow quickly without any extra energy supply from outside of the specimen. In other words, the

propagation of the zone is accelerated beyond this critical point which corresponds to the strongest state of the specimen, i.e. ultimate tensile strength point. After this acceleration takes place, the fibers are quickly broken into small segments in this zone and abruptly lower the supporting load. The fracture of the matrix occurs successively right after the traverse of the zone. The further plastic deformation leading to the failure of the matrix is thought to take place at only limited local regions around the broken fiber ends in the zone. The stress strain curve around the fracture point may be shown schematically as in Fig. 43, if we exaggerate the load drop.

For simplicity, the thickness of this zone, 2b, is assumed to remain constant after the zone starts to propagate quickly. The grip distance is also assumed to remain constant during this quick propagation, because the cross head speed of the testing machine is very low (0.02 inch/min.) compared with the propagating speed, (i.e. the fixed grip condition). Consequently, the load does not do any work, so that dL = 0. The total energy change, dW_t, has to decrease with the increase of zone length, a, in order to propagate without any extra energy increment from outside of the specimen. Then, the critical condition at which the zone can start to propagate spontaneously is stated as the following expression

$$\frac{dW_t}{da} = \frac{d(U + W_z)}{da} = 0 \qquad (20)$$

This statement is obtained by following the Griffith (46) theory for an elliptic crack in a brittle material.

If the length of zone exceeds the critical value at which Eqn. 20 is just satisfied, elastic energy released is more than sufficient

to provide the increment of free energy in the zone, so that the rate of propagation is accelerated.

It is necessary to describe U and W_z in terms of the experimental parameters.

(A) The free energy increment in the fiber failure zone, W_z, Fig. 40, shows the schematic stress distribution in a fiber when it is broken in the zone, where T_o is the stress transfer length outside of the zone. When fibers are broken in the zone, the stress distribution changes from the solid line to the dotted line, releasing extra elastic energy to the surrounding matrix. On the other hand, work is required to break the fibers, and strain the matrix in the zone. W_z can be derived as the summation of these terms.

a) The work per unit thickness, W_m, necessary to deform the matrix in the zone from ϵ_o, the strain in the matrix outside of the zone to ϵ_{futs}, the fibre failure strain, is

$$W_m = V_m \frac{\pi a b}{2} \sigma_m^* (\epsilon_{futs} - \epsilon_o)$$

$$= \frac{\pi V_m a b \sigma_m^* (\sigma_{futs} - \sigma_{fo})}{2E_f} \qquad (21)$$

b) The work, W_f, necessary to strain the fibres in the zone from ϵ_o to ϵ_{futs} is

$$W_f = \frac{V_f \pi a b (\sigma_{futs}^2 - \sigma_{fo}^2)}{4E_f} \qquad (22)$$

c) The released elastic energy from the broken fibres, W_r, is expressed as the difference between the elastic energy of the fibres before their failure and after their failure.

$$W_r = -W_{bef} + W_{aft} \tag{23}$$

where, W_{bef} : elastic energy which the fibres in the zone possess before breakage.

W_{aft} : elastic energy which the fragments of the same fibres in the zone possess after breakage.

$$W_{bef} = \frac{V_f \pi a b \sigma_{futs}^2}{4 E_f} + \frac{V_f a T_o \sigma_{fo}^2}{2 E_f} \tag{24}$$

Where, $$T_o = \frac{r \sigma_{fo}}{\tau} = \frac{T_{uts} \sigma_{fo}}{\sigma_{futs}}$$

Then,

$$W_{bef} = \frac{V_f \pi a b \sigma_{futs}^2}{4 E_f} + \frac{V_f a T_{uts} \sigma_{fo}^3}{2 E_f \sigma_{futs}} \tag{25}$$

$$W_{aft} = V_f \frac{\pi a b}{2} \frac{2}{T_{uts}} \int_0^{\frac{T_{uts}}{2}} \sigma(z) \epsilon(z) dz + V_f a 2 \int_0^{\frac{T_o}{2}} \sigma(z) \epsilon(z) dz$$

$$= V_f a \left\{ \frac{b \pi \tau^2 T_{uts}^3}{2 T_{uts}^3 E_f r^2} + \frac{\tau^2 T_o^3}{3 E_f r^2} \right\}$$

$$= \frac{V_f a}{3 E_f} \left\{ \frac{\pi b}{2} \sigma_{futs}^2 + \frac{T_{uts} \sigma_{fo}^3}{\sigma_{futs}} \right\} \tag{26}$$

then

$$W_r = -W_{bef} + W_{aft}$$

$$= -\frac{V_f\ a\ T_{uts}\ \sigma_{fo}^3}{6\ E_f\ \sigma_{futs}} - \frac{V_f\ \pi\ a\ b\ \sigma_{futs}^2}{12\ E_f} \qquad (27)$$

d) The increment of surface free energy due to the broken fiber ends is negligibly small and will be ignored below.

The sum of these energy terms must be W_z in Eqn. 21.

$$W_z = W_m + W_f + W_r$$

$$= -\left\{\frac{V_f\ a\ T_{uts}}{6\ E_f\ \sigma_{futs}}\right\}\sigma_{fo}^3 - \left\{\frac{V_f \pi a\ b}{4\ E_f}\right\}\sigma_{fo}^2 \left\{\frac{V_m \pi a\ b\ \sigma_m^*}{2\ E_f}\right\}\sigma_{fo} +$$

$$\left\{\frac{V_f \pi a\ b\ \sigma_{futs}^2}{6E_f} + \frac{V_m \pi a\ b \sigma_m \sigma_{futs}^*}{2\ E_f}\right\} \qquad (28)$$

(B) Elastic energy U, released from the region of the specimen outside the elliptic zone due to the formation of the zone.

It is impossible to derive an exact expression for this term lacking a mathematical analysis of the stress and strain in the neighbourhood of the zone; however, it may be possible to derive an approximate expression for this term by modifying Griffith expression for the elastic released energy due to the formation of a two dimensional elliptical crack of length 2a, in an elastic specimen held between rigidly fixed grips under stress, σ.

His theory was later discussed by Knott et al(48) and it was shown that the assumption of rigidly fixed grips is not essential to the Griffith energy criterion for brittle fracture. The same criterion is obtained if the crack propagation is assumed to occur under constant load. In the case of fixed grips, the external forces cannot do work. The critical length of the crack above which it can propagate spontaneously is then determined by the condition

$$dW_c + dU_c = 0 \tag{29}$$

where, dW_c : the free energy required for increasing the length of a crack from $2a$ to $2a + da$,

dUc : the elastic energy released simultaneously in the specimen.

This elastic released energy is given by the Griffith expression

$$dU_c = -d\left\{\frac{\pi(1-\nu^2)\sigma^2(a^2 + b^2)}{E}\right\} \tag{30}$$

in the case of plane strain condition (for thick specimen)

where, ν is Poisson's ratio and E is Young's modulus, and by

$$dU_c = -d\left\{\frac{\pi\sigma^2(a^2 + b^2)}{E}\right\} \tag{31}$$

in the case of plane stress (for thin specimens). In further discussions, only Eqn. 30 is adopted, because the tensile test pieces in the present work are thought to have rather larger thickness (1/3 of the width). The released elastic energy under the fixed grip condition is shown schematically as $\triangle$OAC in Fig. 44.

On the other hand, if the crack propagates while the load is kept constant, the load does work, $|dL|$, shown as $\square$ADBE in Fig. 44. The elastic energy is increased by the amount of dU_c' during this crack propagation. The total

change in potential energy is a decrease of magnitude $|dL| - dU_c'$.
The dU_c' is half of the dL, as $\triangle$BDE shown in Fig. 44, so that half of the external work is stored as additional elastic energy of the specimen, and the other half is available for increasing the free energy of the crack surface, dW_c. The critical condition for this case is expressed in the following equation.

$$dL + dU_c' + dW_c = -dU_c' + dW_c = 0 \qquad (32)$$

Now the relationship between load, L and elongation, S, is given by

$$S = CL \qquad (33)$$

where C is a constant for given crack length, called the compliance of the system. As the change in crack length, da, tends to zero, we may treat C as identical for crack lengths 2a and 2a + da and write,

$$dS = C\,dL \qquad (34)$$

dU_c, dU_c', are given by the following same expressions, using C.

$$dU_c = -\triangle OAC = -\frac{1}{2} S\,dL = -\frac{1}{2} CL\,dL \qquad (35)$$

$$dL - dU_c' = -dU_c' = -\triangle OAB = -LdS + \frac{1}{2}LdS = -\frac{1}{2}LdS = -\frac{1}{2}CL\,dL \qquad (36)$$

For an infinistesimally small amount of crack extension, the decrease in stored elastic energy under the fixed grips condition is identical to the decrease in potential energy under the constant load condition.

Eqn. 29 and 32 show that the energy available for crack propagation at fixed grips is the same as at the constant load, so that even in the latter case, we can use Eqn. 30 to estimate the energy available for the propagation.

$$dL - dU_c' = -dU_c' = -dU = -d\left\{\frac{\pi(1-\nu^2)\sigma^2}{E}(a^2 + b^2)\right\} \qquad (37)$$

(for plane strain condition)

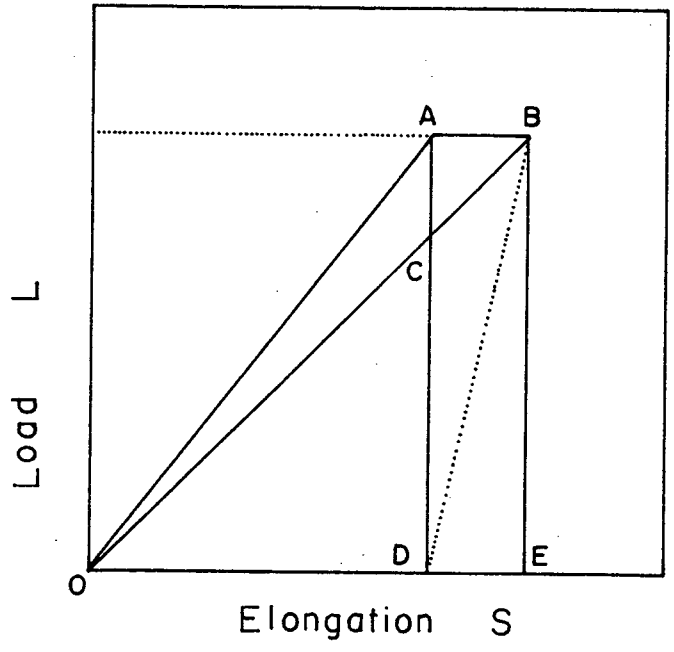

Fig.44. Elastic Loading Curves for Crack Lengths a and a + da.

When a composite specimen fails by tension, (i.e. completely separated into two pieces), under the fixed grip condition, elastic energy which corresponds to the area ΔABC in Fig. 45 is released and the energy $\square$OYAB is stored in the specimen. Although, composites are not perfectly elastic material, if we apply the Griffith released elastic energy expression for their elastic property, an expression for the released elastic energy U_{cc} during the propagation of a crack in a composite is given by

$$U_{cc} = -\frac{\pi (1 - \nu_c^2)\, \sigma_c^2}{E_c} (a^2 + b^2) \qquad (38)$$

where, ν_c : Poissons ratio of the composite

σ_c : stress on the composite

E_c : Young's modulus of the composite

When a fiber failure zone traverses the cross section of a specimen held between fixed grips, the matrix does not fail, but only the fibers are broken into small fragments of average transfer length, T_{uts}, in the zone. Then, the stress drops down from the point A (σ_{crm}), to E (σ_{tz}). The strength of the traversed zone, σ_{tz} , is given by

$$\sigma_{tz} = V_f \overline{\sigma}_{seg} + V_m \sigma_m^* = \frac{1}{2} \sigma_{futs} V_f + \sigma_m^* V_m \qquad (39)$$

During this unloading from A to E, the region outside of the zone shrinks elastically and releases elastic energy which corresponds to the area ΔADE. The amount of this area ΔADE is expressed in the following formula if the gradient of $\overline{Y'E}$ (i.e., the Young's modulus of the zone) is assumed to be $\frac{1}{2} E_f V_f + E_m V_m$.

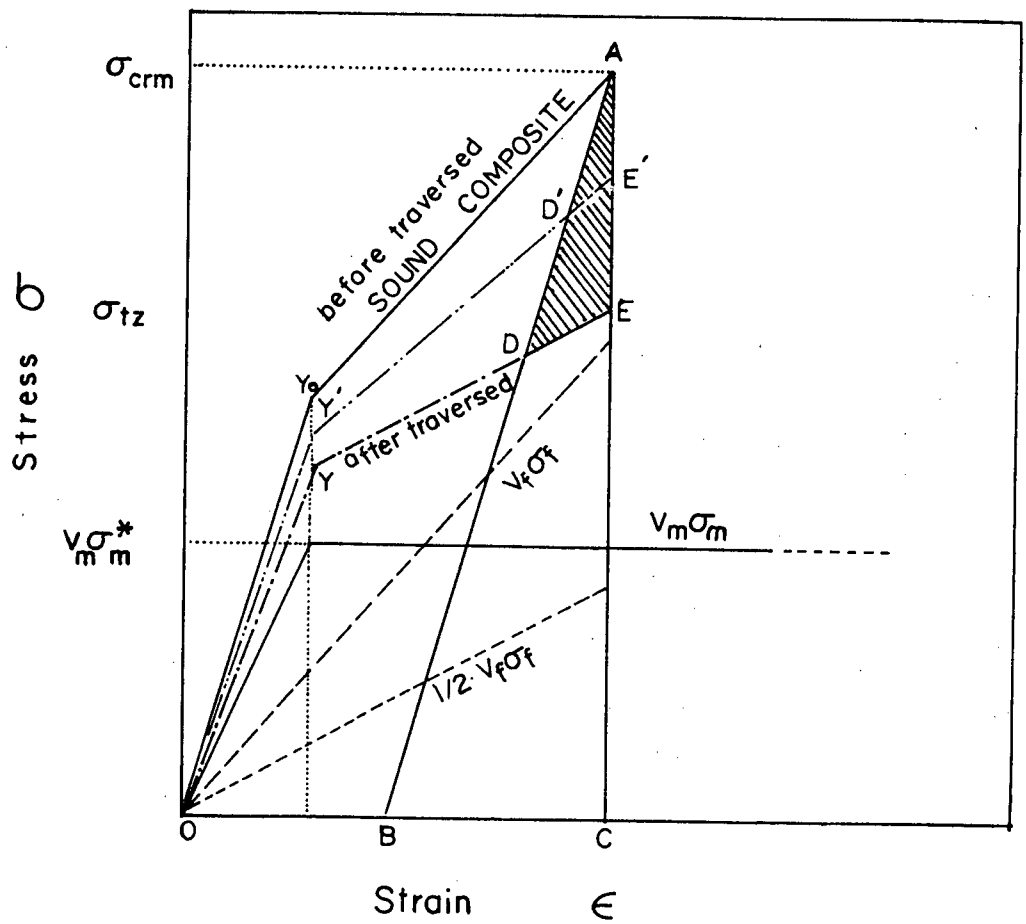

Fig.45. Schematic Diagram of Elastic Energy Released $\triangle$ABC and $\triangle$ADE, when the Crack and the Fiber Failure Zone Traverse the Cross Section

$$\Delta ADE = \frac{(\sigma_{crm} - \sigma_{tz})^2 E_c}{(\frac{1}{2}V_f E_f - V_m E_m)\sigma_{crm}^2} \cdot \Delta ABC$$

$$= \frac{(\frac{1}{2}V_f \sigma_{futs})^2 E_c}{\sigma_{crm}^2 (E_c - \frac{1}{2}V_f E_f)} \cdot \Delta ABC \qquad (40)$$

where, σ_{crm} : composite strength before fiber failure, calculated according to the "rule of mixture".

When the half elliptic fiber failure zone has not yet traversed the full cross section, the energy which corresponds to $\Delta AD'E'$ is released.

In order to modify the Griffith expression for the elastic released energy due to the elliptic crack, U_{cc}, to the elastic released energy due to the half elliptic fiber failure zone, U, we simply assume that U/U_{cc} is proportional to the ratio of the total elastic energy released when the crack and zone completely traverse the full cross section (i.e. $U/U_{cc} = \Delta ADE/\Delta ABC$). U is given by,

$$2U = -\frac{\pi(1-\nu_c)^2 \sigma_c^2 (a^2 + b^2)(\frac{1}{2}V_f \sigma_{futs})^2}{\sigma_{crm}^2 (E_c - \frac{1}{2}V_f E_f)} \qquad (41)$$

Because of the half elliptic shape, U values correspond to the half of U_{cc} in the case of elliptic shape crack (neglecting the effect of the free surface of the half plane).

Substituting σ_{crm},

$$U = -\frac{\pi(1-\nu_c^2) V_f^2 \sigma_{futs}^2 (a^2+b^2)}{8\sigma_{crm}^2 (E_c - \frac{1}{2}V_f E_f)} \left\{ V_f \sigma_{fo}(1-\frac{a}{w}) + \frac{V_f}{2}\sigma_{futs}\frac{a}{w} + V_m \sigma_m^* \right\}^2 \qquad (42)$$

From Eqn.20, $d(W_z+U)/da = 0$, differentiating Eqn. 28 and 42 by a, σ_{fo}, which is the stress in fibers outside of the failure zone at the accelerating point, i.e. the U.T.S. point of the specimen, is given by the following equation.

$$\sigma_{fo}^3+\left\{\frac{3\pi}{2}\frac{b}{T_{uts}}\sigma_{futs}+\frac{3\pi(1-\nu^2)}{2}\frac{E_f}{(E_c-\frac{1}{2}V_fE_f)}\frac{\sigma_{futs}^3}{\sigma_{crm}^2}V_f^3\left(\frac{a}{T_{uts}}-\frac{3a^2}{T_{uts}w}+\frac{2a^3}{T_{uts}w^2}-\right.\right.$$

$$\left.\left.\frac{b^2}{T_{uts}w}+\frac{ab^2}{T_{uts}w^2}\right)\right\}\sigma_{fo}^2+\left\{3\pi\frac{V_m}{V_f}\frac{b}{T_{uts}}\sigma_m^*\sigma_{futs}+\frac{3\pi(1-\nu^2)}{4}\frac{E_f}{(E_c-\frac{1}{2}V_fE_f)}\frac{\sigma_{futs}^4}{\sigma_{crm}^2}V_f^3\cdot\right.$$

$$\left(\frac{3a^2}{T_{uts}w}-\frac{4a^3}{T_{uts}w^2}+\frac{b^2}{T_{uts}w}-\frac{2ab^2}{T_{uts}w^2}\right)-\frac{3\pi(1-\nu^2)}{2}\frac{E_f}{(E_c-\frac{1}{2}V_fE_f)}\frac{\sigma_{futs}^3\sigma_m^*}{\sigma_{crm}^2}V_f^2V_m\cdot$$

$$\left.\left(\frac{2a}{T_{uts}}-\frac{3a^2}{T_{uts}w}-\frac{b^2}{T_{uts}w}\right)\right\}\sigma_{fo}-\left\{3\pi\frac{V_m}{V_f}\frac{b}{T_{uts}}\sigma_{futs}^2\sigma_m^*+\pi\frac{b}{T_{uts}}\sigma_{futs}^3-\right.$$

$$\frac{3\pi(1-\nu^2)}{4}\frac{E_f}{(E_c-\frac{1}{2}V_fE_f)}\frac{\sigma_{futs}^3}{\sigma_{crm}^2}V_f\left[V_f^2\sigma_{futs}^2\left(\frac{a^3}{T_{uts}w^2}+\frac{ab^2}{2T_{uts}w^2}\right)+\right.$$

$$\left.\left.V_fV_m\sigma_{futs}\sigma_m^*\left(\frac{3a^2}{T_{uts}w}+\frac{b^2}{T_{uts}w}\right)+2V_m^2\sigma_m^{2*}\frac{a}{T_{uts}}\right]\right\}=0 \qquad (43)$$

where, $\sigma_c = V_f\sigma_{fo}(1-\frac{a}{w})+V_f\frac{\sigma_{futs}}{2}(\frac{a}{w})+V_m\sigma_m^*$ (44)

$$\sigma_{crm} = \sigma_{futs}V_f+\sigma_m^*V_m \qquad (45)$$

The strength of the composites can be calculated from Eqn. 44, using the σ_{fo} values obtained from Eqn. 43.

IV-2-iii. Improvement of Tensile Strength in Bundle Structure Composites

Graphite fiber reinforced 7178 T6 age hardened alloy composites which have non-uniform, bundle structure, fiber distribution in the matrix as shown in Fig. 15 exhibited higher ultimate tensile strength than uniformly distributed composites. The result was shown in Fig. 22. The increase of the strength may be attributed to the existence of the fiber free regions between fiber concentrated bundles.

These fiber free regions can work as obstacles against the propagation of the fiber failure zone through two possible mechanisms. The thickness of the half elliptic fiber failure zone may be enlarged from 2b to 2h at this fiber free region consuming extra energy as shown in Fig. 46. In addition, such fiber free zone may also act to increase the curvature of the advancing half elliptic zone, thus decreasing the stress concentration at the tip. In the present case, only the first point will be discussed.

Let the average fiber volume fraction be $\bar{V}_f$, the average matrix volume fraction $\bar{V}_m$, the fiber fraction in a bundle, v_f, the matrix volume fraction in a bundle, v_m, and the total number of bundle groups, G, in the cross section of width W and unit thickness. Then we can obtain the following expressions from the geometric relations shown in Fig. 46.

$$\frac{v_f}{\bar{V}_f} = \frac{D^2}{d^2} \tag{46}$$

$$v_m = 1 - \frac{D^2}{d^2}\bar{V}_f \tag{47}$$

The number of groups which the half elliptic zone sweeps, G_z, is given by

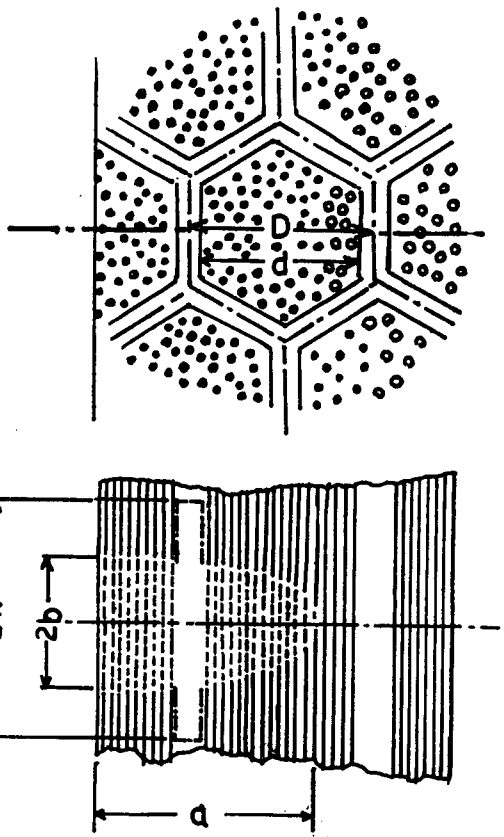

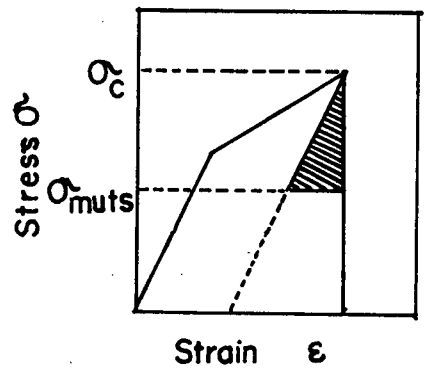

Fig.47. Schematic Stress Strain Curve for a Composite Showing Energy Relationships in Eqn. 56.

Fig.46. Geometry of the Fiber Failure Zone in the Bundle Structure Composite

D : thickness of a hexagonal group

d : thickness of a fiber concentrated area

2b: thickness of the zone (short diameter of the half elliptic zone)

a : advanced distance of the tip of the zone
(length of the half elliptic zone)

2h: thickness of the zone in fiber free region

$$G_z = \frac{a}{w} G \tag{48}$$

The area of a group, A, is given by

$$A = \frac{3\sqrt{3}}{8} D^2 \tag{49}$$

Then

$$\frac{W}{G} = A = \frac{3\sqrt{3}}{8} D^2 \tag{50}$$

The work per unit thickness, W_{mg}, necessary to deform the matrix in the bundles and fiber free zones from ϵ_o to ϵ_{futs} is derived in the following forms. It is thought that the matrix in the fiber free zone can be deformed, on average, up to the fiber failure strain, ϵ_{futs}, in the distance of (h - b) from the edge of the fiber failure zone.

$$W_{mg} = \frac{\pi b}{2} G_z A V_m \sigma_m^* (\epsilon_{futs} - \epsilon_o) + 2(h-b) G_z \frac{3\sqrt{3}}{8} (D^2 - d^2) \sigma_m^* (\epsilon_{futs} - \epsilon_o)$$

$$= \frac{a \sigma_m^* (\sigma_{futs} - \sigma_{fo})}{E_f} \left\{ \frac{\pi b}{2} \bar{V}_m + 2(h-b)\left(1 - \frac{d^2}{D^2}\right) \right\} \tag{51}$$

Substituting for W_m in Eqn. 28 by this W_{mg}, an expression for the free energy increment in the fiber failure zone for a bundle structure composite is obtained. (This corresponds to W_z for the case of a uniform distribution of fibers). Then, the following expression for σ_{fo} at the critical condition of zone length, a , is obtained.

$$\sigma_{fo}^3 + \left\{\frac{3}{2}\pi\frac{b}{T_{uts}}\sigma_{futs} + \frac{3}{2}\pi(1-\nu^2)\frac{E_c}{(E_c-\frac{1}{2}\bar{V}_f E_f)}\frac{\sigma_{futs}^3}{\sigma_{crm}^2}\bar{V}_f^3\left(\frac{a}{T_{uts}} - \frac{3a^2}{T_{uts}w} + \right.\right.$$

$$\left.\left.\frac{2a^3}{T_{uts}w^2} - \frac{b^2}{T_{uts}w} + \frac{ab^2}{T_{uts}w^2}\right)\right\}\sigma_{fo}^2 + \left\{6\sigma_m^*\sigma_{futs}\left[\frac{\pi}{2}\frac{\bar{V}_m}{\bar{V}_f}\frac{b}{T_{uts}} + \frac{2(h-b)}{\bar{V}_f T_{uts}}\left(1-\frac{d^2}{D^2}\right)\right] + \right.$$

$$\frac{3\pi(1-\nu^2)}{4}\frac{E_f}{(E_c-\frac{1}{2}\bar{V}_f E_f)}\frac{\sigma_{futs}^4}{\sigma_{crm}^2}\bar{V}_f^3\left(\frac{3a^2}{T_{uts}w} - \frac{4a^3}{T_{uts}w^2} + \frac{b^3}{T_{uts}w} - \frac{2ab^2}{T_{uts}w^2}\right) +$$

$$\left.\frac{3\pi(1-\nu^2)}{2}\frac{E_f}{(E_c-\frac{1}{2}\bar{V}_f E_f)}\frac{\sigma_{futs}^3\sigma_m^*}{\sigma_{crm}^2}\bar{V}_f^2\bar{V}_m\left(\frac{2a}{T_{uts}} - \frac{3a^2}{T_{uts}w} - \frac{b^2}{T_{uts}w}\right)\right\}\sigma_{fo} -$$

$$\left\{\pi\frac{b}{T_{uts}}\sigma_{futs}^3 + 6\sigma_m^*\sigma_{futs}^2\left[\frac{\pi}{2}\frac{\bar{V}_m}{\bar{V}_f}\frac{b}{T_{uts}} + \frac{2(h-b)}{\bar{V}_f T_{uts}}\left(1-\frac{d^2}{D^2}\right)\right] - \frac{3\pi(1-\nu^2)}{4}\cdot\right.$$

$$\frac{E_f}{(E_c-\frac{1}{2}\bar{V}_f E_f)}\frac{\sigma_{futs}^3}{\sigma_{crm}}\bar{V}_f\left[\bar{V}_f^2\sigma_{futs}^2\left(\frac{a^3}{T_{uts}w^2} + \frac{a\,b^2}{2T_{uts}w^2}\right) + \bar{V}_f\bar{V}_m\sigma_m^*\sigma_{futs}\cdot\right.$$

$$\left.\left.\left(\frac{3a^2}{T_{uts}w} + \frac{b^2}{T_{uts}w}\right) + 2\bar{V}_m^2\sigma_m^{*2}\frac{a}{T_{uts}}\right]\right\} = 0 \qquad (53)$$

The strength of bundle structure composites, σ_c, can be calculated from the following equation, using this σ_{fo} values in Eqn. 53.

$$\sigma_c = \bar{V}_f\sigma_{fo}\left(1-\frac{a}{w}\right) + \bar{V}_f\frac{\sigma_{futs}}{2}\left(\frac{a}{w}\right) + \bar{V}_m\sigma_m^* \qquad (54)$$

IV-2-iv. Estimation of Variables, b and T_{uts}

An attempt was made to estimate the approximate values of the theoretical variables, fiber failure zone thickness, 2b, and stress transfer length in the zone, $T_{uts}/2$, using scanning electron microscope images of the longitudinal section.

The T_{uts} values are independent of the fiber volume fraction, V_f. T_{uts} depends only on the fiber-matrix interfacial shear strength. The T_{uts} value can be estimated as a slightly larger value than the shortest length of fragments **near** the fracture surface in the higher V_f composites. In the case of the lower V_f composites, the broken fiber segments are tilted **near** the fracture surface of specimens as shown in Fig. 30(a). It is more difficult to obtain the values from the micrographs of lower V_f specimens than the higher V_f ones. The higher V_f composites have straight, non-tilted, fiber segments.

The b values cannot be obtained directly from the micrographs. b value can be defined as $b = n\ T_{uts}$ (where n: the average number of segments of a broken fiber near the fracture surface). The n values are not constant and depend on V_f; however, it is also difficult to estimate n values in the micrographs of lower V_f specimens, again because of the same reason. Consequently, for lower V_f specimens, the b values could not be obtained from the micrographs. A treatment to obtain b values for all V_f values using the b values of the higher V_f composites is discussed.

As mentioned before in section III-6, the distance B_f, between the fracture surface and the farthest point, at which broken fiber segments could be observed, was measured. The relation between B_f and V_f and the Young's

modulus were examined and given by the following expression

$$2B_f = K \frac{E_c}{(V_f - V_{fmin})^2} \tag{55}$$

where, K: constant

V_{fmin} is the minimum fiber volume fraction which must be exceeded to strengthen the composite and expressed in Eqn. 7. Combining Eqn. 55 and 7, the following expression is obtained.

$$\frac{(\sigma_c - V_m \sigma_{muts})^2}{2 E_c} 2B_f = \frac{K}{2} (\sigma_f - \sigma_{muts} - \sigma_m^*)^2 \tag{56}$$

If we assume σ_m^* is constant, the right hand side of this equation is constant. This means that the elastic energy necessary to increase the stress in the specimen from $V_m \sigma_{muts}$ to the ultimate strength of the specimen is always constant. This energy is schematically shown as the hatched area in Fig. 47.

If we assume the theoretical average b value varies directly as B_f, we can write the following expression

$$b = \frac{K'}{2} \frac{E_c}{(V_f - V_{fmin})^2} \tag{57}$$

where, K': constant

The proportional constant K' in this equation can be calculated using the b values obtained for the higher V_f composites. Then we can calculate

b values for different V_f using the K' constant. The result of K' calculation is tabulated in Table 11.

Table 11. Observed T_{uts} Values and Calculation Results of K'

Specimen	V_f	T_{uts} inch	n	b inch	K'($lb^{-1}inch^3$)
601T4 #17	0.145	7×10^{-3}	2.0	14.0×10^{-3}	8.74×10^{-12}
201T6 #31	0.17	2.5×10^{-3}	1.6	4.05×10^{-3}	4.17×10^{-12}
7178T6 #38	0.138	2.0×10^{-3}	2.4	4.8×10^{-3}	1.98×10^{-12}

IV-2-v. Evaluation of Ultimate Tensile Strength of Composites by Propagative Fiber Failure Model

The fiber failure zones start to grow at the stress concentrated areas or the defective areas in the specimen. They keep growing larger gradually using the energy which is provided from the applied load until one of them becomes large enough to satisfy the energy criterion obtained in former sections. Then the fiber failure is accelerated and the strength of the composite decreases quickly. Such a point must correspond to the ultimate strength of the specimen.

An attempt was made to calculate the ultimate tensile strength of composites from the equations, with the estimated values of zone thickness, b, and average transfer length T_{uts} in the last section. By fixing the ratio of the zone length, a, and the specimen width, w, at 0, 0.03, 0.05 and 0.10, the strength σ_c of 601 T4 and 201 T6 composites were calculated. In the case of 7178 T6 composites, the a/w ratios, 0, 0.03 were adopted for the calculation. Table 12—15 show numerical values of the parameters which were necessary for the calculations and the calculated results.

These results were superimposed on the experimental data in Fig. 20 — 22. The theoretical curves resulting from the present model are in very much better agreement with the experimental results than is the case for the "rule of mixture" curve, in spite of the considerable scatter of data. Especially in the case of the bundle structure composites of 7178 T6 alloy, the improvement cannot be explained by the "rule of mixture" in which the volume fraction is the only one strength controlling parameter.

The difference among experimental data reported by former workers might

Table 12. Calculation of Strength of 601T4 Composites

a/w	$V_f = 0.17$		$V_f = 0.15$		$V_f = 0.10$		$V_f = 0.06$	
	σ_{fo} ksi	$\sigma_c$ksi	σ_{fo}ksi	$\sigma_c$ksi	σ_{fo}ksi	$\sigma_c$ksi	σ_{fo}ksi	$\sigma_c$ksi
0	238.0	55.4	244.5	52.0	261.0	42.3	273.0	33.3
0.03	185.3	46.3	204.9	45.8	251.1	41.0	272.5	33.0
0.05	160.6	42.15	183.4	42.6	244.6	40.2	272.1	32.4
0.10	116.1	35.3	145.0	37.1	230.1	38.4	272.0	32.0
$E_c x10^6$psi	16.8		16.0		14.0		12.4	
$\sigma_{crm} x10^3$psi	65.9		60.3		46.2		34.9	
b/T_{uts}	0.67		0.90		2.85		(19.69†)	
b/w	0.02		0.028		0.089		(0.613†)	

$E_f = 50 \times 10^6$ p.s.i., $E_m = 10 \times 10^6$ p.s.i. $w = 0.225$ inch $\sigma_{futs} = 300 \times 10^3$ p.s.i.
$\sigma_m^* = 18 \times 10^3$ p.s.i. $\sigma_{muts} = 32 \times 10^3$ p.s.i. $T_{uts} = 7.0 \times 10^{-3}$inch
$K' = 8.74 \times 10^{-12}$ inch^3 / b^{-1} $V_{fmin} = 0.0446$ † : gauge length of the specimen.

Table 13. Calculation of Strength of 201T6 Composites

	V_f = 0.15		V_f = 0.125		V_f = 0.10		V_f = 0.06	
$a/_w$	σ_{fo} ksi	σ_c ksi	σ_{fo} ksi	σ_c ksi	σ_{fo} ksi	σ_c ksi	σ_{fo} ksi	σ_c ksi
0	262.1	80.1	269.2	75.6	276.0	70.8	285.4	62.2
0.03	188.0	68.8	226.3	70.0	257.1	68.6	281.0	61.8
0.05	151.5	63.5	201.8	66.9	245.6	67.3	279.3	61.5
0.10	82.4	54.2	150.8	60.8	219.4	64.4	281.6	61.2
$E_c x 10^6$ psi	16		15		14		12.5	
σ_{crm} ksi	85.8		79.5		73.2		63.1	
$b/_{Tuts}$	1.07		1.67		3.09		22.37	
$b/_w$	0.012		0.0186		0.034		0.249	

$E_f = 50 \times 10^6$ psi, $E_m = 10 \times 10^6$ psi, $w = 0.225$ inch $\sigma_{futs} = 300 \times 10^3$ psi
$\sigma_{m*} = 48 \times 10^3$ psi, $\sigma_{muts} = 60 \times 10^3$ psi, $T_{uts} = 2.5 \times 10\text{-}3$ inch
$K' = 4.17 \times 10^{-12}$ inch^3 lb^{-1} $V_{fmin} = 0.0385$

Table 14. Calculation of Strength of 7178 T6 Composites

	$V_f = 0.15$		$V_f = 0.125$		$V_f = 0.10$	
a/w	$\sigma_{fo} \times 10^3$ psi	$\sigma_c \times 10^3$ psi	$\sigma_{fo} \times 10^3$ psi	$\sigma_c \times 10^3$ psi	$\sigma_{fo} \times 10^3$ psi	$\sigma_c \times 10^3$ psi
0	263.5	87.1	271.6	83.0	278.7	78.3
0.03	174.3	73.6	221.3	76.4	261.6	76.2
$E_c \times 10^6$ psi	16		15		14	
$\sigma_{crm} \times 10^3$ psi	92.6		86.5		80.4	
b/T_{uts}	0.94		1.66		3.95	
b/w	0.0084		0.015		0.035	

$E_f = 50 \times 10^6$ psi $\quad E_m = 10 \times 10^6$ psi $\quad w = 0.225$ inch $\quad \sigma_{futs} = 300 \times 10^3$ psi

$\sigma_m^* = 56 \times 10^3$ psi $\quad \sigma_{muts} = 74.5 \times 10^3$ psi $\quad T_{uts} = 2.0 \times 10^{-3}$ inch

$V_{fmin} = 0.0581$ $\quad K' = 1.98 \times 10^{-12}$ inch^3 lb^{-1}

Table 15. Calculation of Strength of 7178 T6 Bundle Structure Composites

	$\bar{V}_f = 0.19$		$\bar{V}_f = 0.15$		$\bar{V}_f = 0.10$	
a/w	$\sigma_{fo} \times 10^3$ psi	$\sigma_c \times 10^3$ psi	$\sigma_{fo} \times 10^3$ psi	$\sigma_c \times 10^3$ psi	$\sigma_{fo} \times 10^3$ psi	$\sigma_c \times 10^3$ psi
0	281.6	98.9	289.3	91.0	284.0	78.8
0.03	203.6	83.7	258.2	85.8	271.0	77.1

$E_c \times 10^6$ psi	17.6	16	14
$\sigma_{crm} \times 10^3$ psi	102.4	92.6	80.4
b/T_{uts}	0.50	0.94	3.95
b/w	0.000225	0.0084	0.0035

$E_f = 50 \times 10^6$ psi $\quad E_m = 10 \times 10^6$ psi $\quad w = 0225$ inch

$\sigma_{futs} = 300 \times 10^3$ psi $\quad \sigma_m^* = 56 \times 10^3$ psi $\quad \sigma_{muts} = 74.5 \times 10^3$ psi

$T_{uts} = 2 \times 10^{-3}$ inch $\quad \bar{V}_{fmin} = 0.0581$ $\quad K' = 1.98 \times 10^{-12}$ inch^3 lb^{-1}

$\frac{d}{D} = 0.85^{\dagger}$ $\quad h = 12 \times 10^{-3}$ inch

(† This value was estimated from Fig. 15)

be also understood by this theory. The composites fabricated by the infiltration technique showed much higher fiber strengthening efficiency than by the other fabrication techniques, such as the chemical vapour deposition method. The composites fabricated by the infiltration process are thought to possess the bundle structure distribution inevitably.

It was found that not only the factor, V_f, used in the "rule of mixture" but also other new factors, such as E_c, the fiber distribution, and the zone thickness, 2b, have an influence on the strength of composites. The deformation characteristics of the matrix, the fiber diameter, and the fiber spacing are thought to control the zone thickness, 2b.

Listed below are some problems that still remain, concerning the present model.

1) The shear stress, τ, was assumed to have the same value in the region outside and inside of the zone, because the work hardening effect of the matrix was neglected. The actual stress strain curve of the matrix alloy does show work hardening.

2) The present equations were obtained, assuming the fiber failure zone has a half elliptic shape. This equation cannot be applied when the half zone thickness is larger than the length ($b > a$). The calculated curves for lower V_f values are incorrect. These parts are shown in dotted lines.

3) Some ambiguity exists in the method to obtain average transfer length, average number of fragments and the zone thickness.

4) We cannot obtain the strength of composites from this model unconditionally as long as the exact values of the zone length, a, at the accelerating point are not known.

IV-3. Characteristics of Powder Slip Interpretation Method

It has been very difficult to fabricate graphite fiber reinforced metal composites because of the small fiber diameter. In the present work, a very unique process was developed in order to make uniformly distributed fiber composites; however, some problems still remain. The following characteristics of this process can be pointed out.

1) Blended powders of different elements cause the scatter of matrix composition in the green composites, because each element powder has a different settling speed in the process. If alloy powders can be used, this problem will be solved.

2) Effective interpenetration is dependent on the relative sizes of fibers and powder particles. The more nearly equal these dimensions are, the higher the volume fraction that can be made.

3) This process can be applied to fabricate composites of many other fiber-metal systems because the wetting property of the two components is not necessary for this process.

4) This process is more suitable to produce composites of large structural components than are the other processes such as infiltration and coating, because the size of a fiber bundle which is prepared prior to the operation of this process, can be increased without any problems. In the case of the infiltration and coating processes, the size of a bundle for the operation is limited. The composite wires have to be first fabricated prior to hot pressing to fabricate the composite structure.

5) On the other hand, it is difficult to fabricate the composites of bundle structure which can be expected to have higher strength than uniformly

distributed composites according to the present theory. The infiltration process seems to have a greater advantage than the present process from this point of view.

V SUMMARY AND CONCLUSIONS

1) A new fabrication technique has been developed to fabricate graphite fiber reinforced aluminum alloy composites of 5% – 17% fiber volume fractions, using metal powder slip and continuous graphite fibers.

2) The strength of these composites is lower than the "rule of mixture" value as other workers have reported previously.

3) A "fiber failure zone" propagation model has been proposed and verified by observations of fiber fracture behaviour.

4) An energy criterion has been formulated for the accelerated propagation of the zone in the specimen, and the ultimate tensile strength of these composites is thought to correspond to this accelerating point. The experimental strength data shows better correlation with this propagative fiber failure model than the "rule of mixture" model.

5) This model suggests the possibility of improving the strength by producing a bundle structure fiber distribution in the composite instead of a uniform fiber distribution.

6) This model shows that, in addition to fiber volume fraction, the zone thickness is also a strength controlling factor. The zone thickness seems to be related indirectly with other factors such as the fiber diameter, fiber spacing, deformation property of the matrix, and the matrix-fiber bond strength.

VI SUGGESTION FOR FUTURE WORK

Some lines of future investigation can be suggested from the discussion of the present work.

1) In order to obtain the average zone thickness properly, the distribution of strain in the matrix has to be measured.

2) A more exact mathematical treatment for the energy change due to the zone formation has to be performed.

3) A method to obtain the exact average lengths of fiber fragments in the zone has to be developed.

4) The zone length change during the tensile test has to be measured in order to know the factors which influence it.

REFERENCES

1. A. Kelly and G.J. Davies, Met. Rev., 10 (1965), p.1.
2. P.W. Jackson, D.M. Braddick, and P.J. Walker, Fib. Scien. Techn., 5 (1972), p.219.
3. W.H. Sutton, "Whisker Technology", Edited by A.P. Levitt, Wiley-Interscience (1970), p.273.
4. H. Hahn, A.P. Direcha, P. Lare, and B. Dennison, "Research on Whisker Reinforced Metal Composites", Final Technical Report AFML-TR-67-296, September 1967.
5. I. Ahmad, V.P. Greco, and J.M. Barranco, J. Comp. Mater., 1 (1967), p.18.
6. A.A. Baker, A. Martin, and R.J. Bache, Composites, 2(1971), p.154.
7. C.M. Jackson and H.J. Wagner, "Fiber-reinforced Metal-matrix Composites: Government Sponsored Research, 1964-1966".
8. J.A. Alexander, J.C. Whiters, and B.A. Macklim, "Investigation of Three Classes of Composite Materials for Space Vehicle Application", in Advanced Fibrous Materials, SAMPE, 10 (1966), paper B-6.
9. A.A. Baker, Mat. Scien. Engin., 17 (1975), p.177.
10. D.E. Niesz, J. Fleck, C. Kistler, and I. Machlin, Proc. AIAA Struct. Mater Conf., 9th., Paper 68-338.
11. I.J. Toth, W.D. Brentnall, and G.D. Menke, "Composite: State of the Art", Editre by J.W. Weeton and E. Scala, AIME (1971), p.139.
12. F.D. Lemkey, R.W. Hertzberg, et al. Trans. AIME, 233 (1965) p.334.
13. M. Salkind, F.D. Lemkey, SAMPE, 10 (1966), paper F-35.

14. G. Garmong, Met. Transaction 6A (1975). p.1335.

15. F.D. Lemkey and M.J. Salkind, "Crystal Growth", Edited by H.S. Peiser, Proceeding of an International Conf. on Crystal Growth, Boston, June 1966, Pergamon Press (1967), p.171.

16. E.R. Thompson and F.D. Lemkey, "Composite Materials", Edited by A.G. Metcalfe, Academic Press (1974), Vol.4, p.101.

17. K. Esashi and S. Koda, "Quantitative Relation Between Properties and Microstructure", Proc. International Conf. at Haifa (1969), p.243.

18. S. Goto, K. Esashi, S. Koda, and S. Morozumi, J. Japan Inst. Metals, 37 (1973), p.466.

19. J.C. Williams and G. Garmong, Met. Trans. 6A (1975), p.1699.

20. E.R. Thompson, D.A. Koss, and J.C. Chesnutt, Met. Trans. 1 (1970), p.2807.

21. J.C. Hubert, W. Jurz, and B. Lux. "Etude Exploratoire des Systems Ni_3 Al-Ni_3Ta et NiAl-$NiAlNb$, Final Rep. DRME Contract No. 69-537.

22. F.D. Lemkey and E.R. Thompson, Met. Trans. 2 (1971), p.1537.

23. R.T. Pepper, J.W. Upp, R.C. Rossi, and E.G. Kendall, Met. Trans. 2 (1971), p.117.

24. R.T. Pepper and R.A. Penty, J. Composite Mater., 8 (1974), p.29.

25. E.G. Kendall, "Composite Materials", Edited by A.G. Metcalfe, Academic Press (1974), Vol. 4, p.319.

26. W.H. Sutton and J. Chorne, "Fiber Composite Materials", ASM (1964), p.173.

27. R.L. Mehan, ASTM. S.T.P. No. 438 (1968), p.29.

28. A. Kelly and W.R. Tyson, J. Mech. Phys. Solids, 13 (1965), p.329.

29. G. Blankenburgs, J. Australian Inst. Metals, 14 (1969), p.236.

30. A.W.H. Morris, "Carbon fibers: their composition and applications", Intern. Conf. (1971), London, Paper 17.

31. R.G. Shaver, "Composite Materials in Engineering Design", A.S.M. (1972), p.232.

32. K.G. Krieder, "Composite Materials", Vol.4, p.399. Academic Press.

33. G.R. Sippel and M. Herman, "Composites: State of the Arts", A.I.M.E. (1971), Edited by J. Weeton and E. Scala, p.211.

34. C.A. Calow and R.J. Wakelin, J. Inst. Metals, 96 (1968), p.147.

35. H.N. Barr, "Investigation of Silicon Carbide Whisker Reinforced Metal Matrix Composites", Final Technical Report AFML-TR-67-296, September 1967.

36. L.C. Wohrer and J. Economy, SAMPE, 10 (1966), Paper B-6.

37. A.P. Divecha, P. Lare, and H. Hahn, "Silicon Carbide Whisker-Metal Matrix Composites", Tech. Rpt. AFML-TR-67-321, October 1967.

38. P.J. Lare, A.P. Divecha, and H. Hahn, "Research on Whisker Reinforced Metal Composites", Final Report Contract NOOO-19-67-Go404, July 1968.

39. R.J.E. Glenny, J.E. Northwood, and A. Burwood-Smith, Intn. Metallurgical Review, 20 (1975), p.1.

40. P.W. Jackson, Metals Eng. Quart., 9 (1969), p.22.

41. A. Kelly and W.R. Tyson, J. Mech. Phys. Solids, 13 (1965), p.320.

42. H.L. Cox, Brit. J. Appl. Phys., 3 (1952), p.72.

43. M.R. Piggott: Acta Met., 14 (1966), p.1429.

44. Miura and Okuno, J. Japan Inst. Metals, 34 (1970), p.1201.

45. J.H. Steel and H.W. Herring, "Failure Mode in Composites", AIME (1972), p.343.

46. A.A. Griffith, Phil. Trans. R. Soc., A221 (1920), p.163.

47. S. Koda, Trans. Japan Inst. Metals, 15 (1974), p.381.

48. J.F. Knott, "Fundamentals of Fracture Mechanics", London Butterworth (1973).

E. Orowan, Welding Research Supplement, March, (1955), p.157.